

**Texas A&M University
Mechanical Engineering Department
Turbomachinery Laboratory
Tribology Group**

**STRUCTURAL FORCE COEFFICIENTS FROM METAL MESH PADS
FOR A FOIL BEARING**

Research Progress Report to the TAMU Turbomachinery Research
Consortium

TRC-B&C-02-2016

by

Luis San Andrés
Mast-Childs Chair Professor
Principal Investigator

Travis Cable
Research Assistant

May 2016

STRUCTURAL FORCE COEFFICIENTS FROM METAL MESH PADS FOR A FOIL BEARING

TRC Project, TEES # 400124-00078

EXECUTIVE SUMMARY

The following report relates an improved manufacturing process for metal mesh pads. The manufacturing process yields five metal mesh pads, four of which show markedly similar dimensions and structural coefficients (stiffness and material loss factor). Results show that pad thickness measurements, conducted with common measurement tools such as calipers or micrometers, are both inaccurate and unnecessary when compared to a pad “first-touch” thickness. A pad “first-touch” thickness determines the thickness of a pad for a known static load (0.45 N in the following report), providing a more accurate metric.

A test rig for the static and dynamic load performance of metal mesh pads determines the static load vs. deflection as well as the structural stiffness and material loss factors for the five copper mesh pads. The pads display a piece-wise linear stiffness, as determined from the static load vs. deflection measurements, displacing nearly 0.75 mm for small loads (less than 100 N). Dynamic load measurements show that the pads are quite similar, with the exception of Pad #1, having an average structural stiffness of ~ 1.75 MN/m and a loss factor of ~ 0.2 . Increasing the pad preload increases both the real and imaginary parts of the complex stiffness (\bar{F}/\bar{X}), increasing the pad stiffness by a factor of 4 for applied preloads from 30-120 N. The increase in preload, however, does not affect the pad loss factor, remaining at ~ 0.2 . In addition, the pad structural stiffness decreases linearly with increasing amplitudes of motion and a fixed preload of 60 N. Again, the increase in motion amplitude does not affect the loss factor, staying at ~ 0.2 .

The end of the technical report shows briefly the design of a thrust bearing test rig for determining the static and dynamic load performance of thrust bearings with outer diameters (ODs) as large as 113 mm (4.15 in) and specific loads up to 207 kPa (30 psi). A purchased liquid cooled, industrial router motor and variable frequency drive (VFD), capable of a shaft speed up to 40 krpm (~ 190 m/s surface speed), sits ready for implementation in either a radial or thrust bearing test rig. Future work intends to improve the test rig for metal mesh pads as well as performing tests on an assembled radial metal mesh bearing. Machining of the thrust bearing test rig will begin upon completion of the design phase.

TABLE OF CONTENTS
STRUCTURAL FORCE COEFFICIENTS FROM METAL MESH PADS FOR A FOIL BEARING

Luis San Andrés and Travis Cable, May 2016

LIST OF TABLES

#	<u>page</u>
Table 1. Bearing cartridge and rotor dimensions.....	5
Table 2. Designed properties and dimensions of metal mesh pads.....	6
Table 3. Pad compressed thicknesses (undetermined compressive loads applied). Thickness measurements in mm.....	12
Table 4. First-touch thicknesses of five manufactured metal mesh pads (applied load = 2.22 N).....	15
Table 5. Coefficients of polynomials fitting recorded deflection and load data.....	16
Table 6. Metal mesh pad stiffness for five manufactured metal mesh pads. Dynamic motion amplitude of 20 μm peak-peak and ~ 60 N ($W/A_{\text{pad}} = 14$ kPa) of preload. Frequency range $\omega_e = 0\text{-}300$ Hz.....	25
Table A.1 Real parts of the complex stiffness and their associated precision uncertainties for a confidence interval of 95%. Pad #5, $ X = 10$ μm , $W = 60$ N.....	41
Table A.2 Equivalent stiffness and mass for Pad #5 and associated uncertainties for a 95% confidence interval. $ X = 10$ μm , $W = 60$ N.....	42
Table A.3 Material loss factors and their associated precision uncertainties for a confidence interval of 95%. Pad #5, $ X = 10$ μm , $W = 60$ N.....	43

LIST OF FIGURES

#	<u>page</u>
Figure 1. Depiction of a metal mesh pad (dimensions in mm).....	4
Figure 2. Schematic view of a five pad metal mesh bearing. Dimensions shown in mm. .	5
Figure 3. 16 Copper mesh gauze manufactured by TWP Inc. [15].	7
Figure 4. Photograph of a wooden jig for folding metal mesh pads.....	8
Figure 5. Folding process of a metal mesh pad in a dedicated wooden jig.	8
Figure 6. Schematic views of a metal jig for forming metal mesh pads. Dimensions in mm.	9
Figure 7. Compression of a metal mesh pad in a dedicated jig.	9
Figure 8. Schematic views of a test rig for loading a formed metal mesh pad.	10
Figure 9. (a) Photograph of a metal mesh pad including measurement locations and (b) a photograph of a thickness measurement taken at location 2.....	11
Figure 10. Metal mesh test rig installed in a vertical mill for static load testing.....	13
Figure 11. Obtaining a datum for thickness measurements with the metal mesh test rig installed in a vertical mill.....	14
Figure 12. Specific load (W/A_{pad}) versus displacement for five metal mesh pads.....	15
Figure 13. Metal mesh structural stiffness versus mesh displacement.	17
Figure 14. Metal mesh test rig assembled for dynamic load measurements.	18
Figure 15. Schematic view of the metal mesh test rig and corresponding single degree of freedom model.	19
Figure 16. Schematic views of the sliding assembly for free-free impact tests.....	20
Figure 17. (a) Measurements of sliding assembly vibration versus time and (b) corresponding frequency spectrum.	21
Figure 18. Measured (a) force (b) displacement and (c) acceleration versus time for Pad #5. $\omega_e = 210$ Hz, $W/A_{pad} = 14$ kPa.....	22
Figure 19. Comparison of measured and derived amplitudes of acceleration versus frequency for Pad #5. $W = 60$ N, $ X = 10$ μ m.....	23
Figure 20. (a) Real part and (b) imaginary part of the complex stiffness versus excitation frequency for five metal mesh pads. $W/A_{pad} = 14$ kPa, $ X = 10$ μ m.	24

Figure 21. Material loss factor versus excitation frequency for five manufactured metal mesh pads. $W = 60$ N, $|X| = 10$ μ m. 26

Figure 22. Photograph of Pad #1 installed in the metal mesh test rig for dynamic testing and with an applied preload of $W/A_{pad} = 21$ kPa. 27

Figure 23. (a) Real part and (b) imaginary part of the complex stiffness versus excitation frequency for Pad #5 and increasing preload. $|X| = 10$ μ m. 29

Figure 24. Identified MM Pad #5 stiffness coefficients versus applied preload. Results obtained for single frequency excitation from 30-300 Hz and a motion amplitude of $|X| = 10$ μ m. 30

Figure 25. Loss factor for Pad #5 versus excitation frequency for increasing preloads. $|X| = 10$ μ m. 31

Figure 26. Metal mesh stiffness coefficient versus dynamic motion amplitude for Pad #5. $W/A_{pad} = 14$ kPa. 32

Figure 27. Material loss factor versus excitation frequency for Pad #5 and increasing dynamic motion amplitudes. $W = 60$ N. 33

Figure 28. A (a) photograph and (b) a schematic view of an assembled metal mesh foil bearing with five metal mesh pads ($t_{MM} = 7.36$ mm). 34

Figure 29. Photograph of a purchased 40 krpm, 3 HP motor, controller and dedicated chiller. 35

Figure 30. Schematic view of envisioned test rig for the static and dynamic evaluation of thrust foil bearings. 36

Figure 31. (a) Schematic and (b) cross section views of the static loading plenum and shaft for a thrust bearing test rig. 37

NOMENCLATURE

\bar{A}	FFT of measured acceleration [(N.m)/s ²]
A_{pad}	Metal mesh pad surface area [m ²]
CR	Metal mesh compactness ratio ($CR = m_{MM} / (\rho_{MM} V_{MM})$) [-]
C	Damping coefficient [(N.s)/m]
c_d	Bearing diametral clearance [mm]
D	Diameter [mm]
D_1, D_2	Outer and inner diameters of a metal mesh pad [mm]
E	Modulus of elasticity [GPa]
\bar{F}	FFT of measured force [N]
f_s	Sampling frequency [Hz]
K	Linear stiffness coefficient [N/m]
i	Imaginary unit $i = \sqrt{-1}$
L	Length [mm]
M	Mass [g]
R	Radius [mm]
T	Thickness [mm]
t	Time [s]
U	Uncertainty [μ m, N]
V	Volume [mm ³]
\bar{X}	FFT of measured displacement [m]
x	Displacement [m]
W	Applied load/preload [N]
γ	Material loss factor $\gamma = \text{Im}(\bar{F} / \bar{X}) / K_{MM}$
φ	Metal mesh pad circumferential extent [°]
ρ	Density [g/cm ³]
ω	Excitation frequency [rad/s]

SUBSCRIPTS

C	Cartridge
$copper$	Copper material
i	Inner
L	Load
MM	Metal mesh
o	Outer
R	Rotor
t_f	Top foil

PROJECT GOALS, TASKS AND THEIR COMPLETION

TRC funds a two-year research program to bring the technology of metal mesh foil bearings (radial and thrust) to a commercialization level. The deployment of microturbomachinery (MTM) supported on metal mesh foil bearings (MMFBs) relies on overcoming intermittent contact and damaging wear during rotor start up and shut down, temporary rubs during normal operating conditions; and most importantly, with an engineered thermal management, to ensure reliable performance in environments with large heat generation (as in permanent magnet motors). The proposed tasks in 2015-2016 are:

- (a) Construct metal jigs to manufacture identical metal mesh pads.
- (b) Determine a more accurate means of classifying metal mesh pad dimensions and verification of assembled bearing clearances.
- (c) Design a novel thrust metal mesh foil bearing.
- (d) Overhaul an existing test rig for testing of thrust (metal mesh) foil bearings.
- (e) Measure rotor lift-off speed and break away torque, touchdown speed and stall torque, load versus minimum film thickness, and drag power losses, over a range of shaft speeds to 25 krpm.

Tasks (a) and (b) are complete, while (c)-(e) are still in progress. The project initially intended to construct two inexpensive rigs (task (d) above) for testing of radial and thrust MMFBs. However, an available commercial router motor (max speed 25 krpm) does not have the required torque nor a controller to maintain steady rotor speed during tests with the large radial MMFB. Purchasing a new motor (max speed 40 krpm), dedicated variable frequency drive and chiller dictates the redesign of the previously proposed test rigs. The end of this report briefs on the motor as well as a thrust bearing test rig, currently in the final stages of its design process.

BRIEF REVIEW OF RELEVANT LITERATURE

Childs [1] first identified metal mesh as a viable material for damping in an analysis for the space shuttle main rocket engine turbo pump. Later, Dr. John Vance and students [2-4] present experiments with metal mesh dampers (MMDs), quantifying their stiffness and damping with varying amounts of axial and radial preload as well as in increased temperatures and with oil entrainment. Vance's experiments show that MMDs have material damping equal to (or even higher than) the viscous damping provided by similar size oil film dampers, highlighting the useful properties of metal mesh. The work prompted the investigation of wire metal mesh in compliant gas foil bearings as it is low cost and currently not patented.

San Andrés and Chirathadam [5,6] extend the work of Vance, being the first utilizing a continuous metal mesh layer as the underspring structure in a purely hydrodynamic gas foil bearing. The small sized (45 mm ID) MMFB displays performance (drag power loss and temperature rise) similar to that of a commercial first generation bump foil bearing (BFB). In addition, dynamic load tests over a limited frequency range (0-400 Hz) show that the MMFB has a material loss factor (material damping) nearly twice that of a similar BFB.

Ertas [7] continues the work on metal mesh dampers, determining the material damping for different MMDs. Dynamic load tests show that nickel titanium shape memory alloy MMDs have superior damping, when compared to steel, Inconel and copper dampers. Ertas [8] also implements two MMDs as the compliant and energy dissipation structure in a hybrid gas bearing design. The hybrid gas bearing comprises of four pads, connected to the bearing cartridge via integral s-springs, which allow the pads to tilt angularly and displace radially. The two MMDs locate on both axial ends of the bearing cartridge, between the tilting pads and their housing. The bearing has a diameter of 110 mm and a length of ~85 mm. The author indicates that maximizing the stiffness ratio between the gas film and the compliant mesh structure enhances effective damping from the support structure.

Delgado [9] identifies the dynamic force coefficients for the compliant hybrid gas bearing from Ref. [8] for operation with a specific load of 140 kPa (20 psi), showing their frequency dependency and variation with increasing supply pressure. Results show that

increasing the bearing supply pressure increases the direct stiffness of the bearing, but decreases its direct damping. The cross-coupled coefficients are small. In addition to dynamic load tests with no rotor speed, imbalance response tests with up to four times the API 610 permissible imbalance ($u = 4W/N$) show that the bearing can sustain large amplitude motions.

Santiago and Solórzano [10] show the promise of implementing metal mesh as the underspring structure in large (90 mm ID) hydrodynamic gas foil bearings. The authors examine two similar MMFBs, supporting a 29 kg rotor ($W/LD = 20$ kPa, 3 psi) on a dedicated test stand, with the goal of replacing the gas seals in a small, five-stage centrifugal compressor. Test results show that the compressor runs smoothly up to the maximum speed of 9 krpm (surface speed $R\Omega = 42.5$ m/s), then experiences subsynchronous vibrations at approximately half the shaft speed. The drive-end (DE) MMFB fails. The authors attribute the bearing failure to a loosening and consequent removal of the DE bearings' top foil, ultimately pointing to poor bearing construction and a lack of safety guidelines.

Feng *et al.* [11,12] continue to investigate metal mesh as a viable source of damping in gas foil bearings. The material damping (hysteric and frictional in nature) in a metal mesh structure is complex in nature and requires accurate models (as in [11,12]) or experiments to determine.

The following report details an updated manufacturing process for metal mesh pads and presents experimentally determined structural force coefficients for several metal mesh pads for increasing mechanical preloads and an increasing dynamic motion amplitude.

MANUFACTURING METAL MESH PADS FOR A FOIL BEARING

A goal for the current project is to develop the methods and means for manufacturing metal mesh pads with consistent geometry and physical structural properties. In prior MMFB research at TAMU, major uncertainties in manufacturing identical metal mesh pads due to (a) using low cost commercial mesh with inconsistent dimensions, and (b) a lack of effective tools for compressing uniformly a metal mesh pad. A prior TRC report

[13] shows that 3D-printing jigs to form metal mesh pads are ineffective, due to the flexibility and large imposed pressures for molding a metal mesh pad.

DESCRIPTION OF PADS AND BEARING

Table 1 displays the geometry of the metal mesh bearing cartridge, a stainless steel top foil, and the steel journal. The dimensions of the MMFB and test rotor are identical to those in Ref. [10]. The bearing cartridge is manufactured of common 4140 steel, while the top foil is constructed of 0.25 mm [10 mil (+/- 0.5 mil)] thick stainless steel shim stock. The steel journal has a low friction Teflon coating (127 μm) applied to the OD, over ~92 mm of its axial length.

Figure 1 displays the design dimensions for a metal mesh pad which makes the underspring structure for a MMFB. Five metal mesh pads of thickness $t_{MM} = 7.36$ mm are constructed for the MMFB described herein each having an axial length of 81.3 mm and a circumferential extent of 67° .

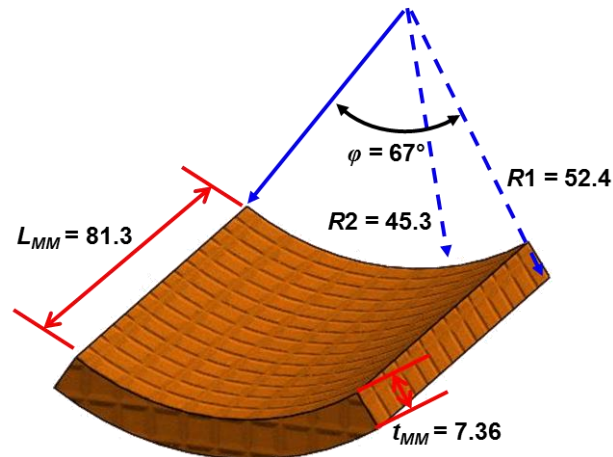


Figure 1. Depiction of a metal mesh pad (dimensions in mm).

Table 1. Bearing cartridge and rotor dimensions.

Parameter	Magnitude	Unit
Rotor mass, M_R	3	kg
Diameter, $D_{o,R}$	90.17	mm
Length, L_R	101.6	mm
Bearing cartridge mass, M_C	6.75	kg
Outer diameter, $D_{o,C}$	166.6	mm
Inner diameter, $D_{i,C}$	105.4	mm
Axial Length, L_C	81.3	mm
Top foil material	Stainless 316	-
Top foil thickness, t_{tf}	0.254	mm
Length, L_{tf}	327	mm
Elastic modulus, E_{tf}	214	GPa

Figure 2 displays a schematic view of a MMFB assembled with five copper metal mesh pads. Note in Figure 2, the clearance (if existing) between the journal and the top foil is magnified for clarity only.

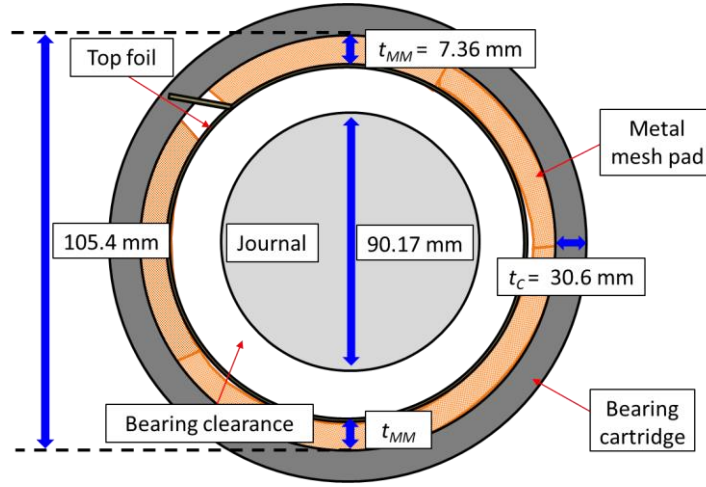


Figure 2. Schematic view of a five pad metal mesh bearing. Dimensions shown in mm.

For a given pad thickness, the resulting diametral clearance (c_D) for the MMFB follows from

$$c_D = D_{i,C} - D_{o,R} - 2t_{tf} - 2t_{MM} \quad (1)$$

here t_{MM} is the thickness of the metal mesh pads, $D_{i,C}$ is the inner diameter of the bearing cartridge, $D_{o,R}$ is the outer diameter of the journal and t_{tf} is the thickness of the top foil. In

a typical foil bearing, the journal rests, and compresses, on the bearing top foil until its rotation develops a hydrodynamic pressure that displaces the top foil and underspring structure, thus creating a small gap between the rotor and smooth top foil.

The thickness of a metal mesh pad which produces a null clearance is $t_{MM} = 7.36$ mm. The volume of a metal mesh pad is given by

$$V_{MM} = \pi \left(\frac{\varphi}{360} \right) \left(\frac{D_1^2 - D_2^2}{4} \right) L_{MM} \quad (2)$$

where φ is the arc extent of a pad, L_{MM} is the axial length of a pad, and D_1 and D_2 are the outer and inner diameters of a pad, respectively. With a thickness of $t_{MM} = 7.36$ mm, the pad volume equals $V_{MM} = 34.3$ cm³. In addition, the surface area of the pad (A_{pad}) is

$$A_{pad} = \pi \left(\frac{\varphi}{360} \right) \left(\frac{D_2^2}{4} \right) L_{MM}.$$

A pad compactness ratio (CR) relates the mass of a pad (m_{MM}) to its full mass density ($\rho_{copper} \times V_{MM}$), i.e.

$$CR = \frac{m_{MM}}{\rho_{copper} V_{MM}} \quad (3)$$

The literature on MMFBs and metal mesh dampers (MMDs) [2,3,4,14] shows that a $CR \geq 30\%$ is desirable obtaining considerable material damping. Thus, the pads herein are designed for **$CR = 30\%$** . Table 3 displays the designed dimensions for the copper mesh pads.

Table 2. Designed properties and dimensions of metal mesh pads.

Parameter	Symbol	Magnitude
Density of Copper (20 °C)	ρ_{MM}	8.94 g/cm ³
Wire Diameter	ϕ_{MM}	0.28 mm
Length	L_{MM}	81.3 mm
Inner Radius	R_2	45.34 mm
Outer Radius	R_1	52.7 mm
Circumferential Extent	φ	67°
Thickness	t_{MM}	7.36 mm
Pad Area	A_{pad}	43.12 cm ²
Mass	m_{MM}	91.8 g

PAD FORMING PROCEDURE

Figure 3 displays a strip length of industrial copper mesh gauze, with properties listed. Although the mesh and material are not made specifically for MMFBs, they have a constant mesh density and consistent weight per square foot equal to 6.7 N/m^2 (0.14 lb/ft^2), which makes them ideal for manufacturing mesh pads. The copper wire has 0.28 mm diameter and the square openings have equal length and width of 1.3 mm .

Parameter	Magnitude
Opening	1.3 mm
Weight per square foot	6.7 N/m^2
Density of copper	$8,940 \text{ kg/m}^3$

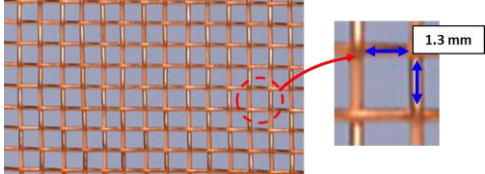


Figure 3. 16 Copper mesh gauze manufactured by TWP Inc. [15].

The mass (m_{MM}) to obtain $CR= 30\%$ for the pads is $91.8 (\pm 0.2)$ gram.

$$m_{MM} = CR(\rho_{copper} V_{MM}) \quad (4)$$

To begin forming the copper mesh pads, a section of copper mesh with a width of 81.3 mm and length of $\sim 152 \text{ cm}$ is cut out of a larger strip sheet of mesh, as seen in Figure 5. The mesh strip is weighed and cut; and in an iterative process will achieve the desired mass of 91.8 gram .

Once the metal mesh length has the appropriate weight, the length is rolled in a dedicated wooden jig, end-over-end, as shown in Figure 4. Rolling consistent metal mesh pads is a challenging endeavor, nearly impossible without the aid of a constraining device. When rolling a metal mesh pad from a length of wire mesh, the folds tend to become skewed (non-parallel). To rectify this tendency, Figure 4 displays a wooden jig which maintains the pads' parallelism throughout the folding process. This wooden jig also ensures that each pad, when folded, has (identical) axial length of $\sim 8.13 \text{ cm}$.

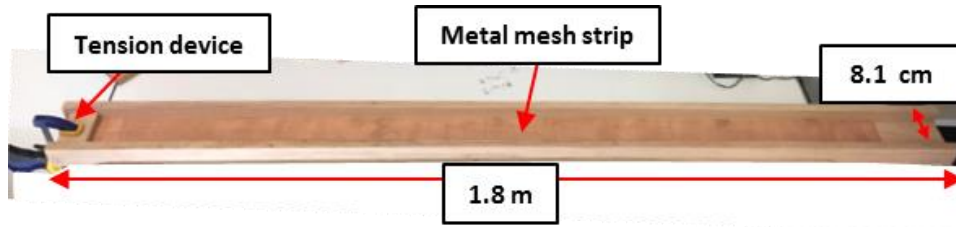


Figure 4. Photograph of a wooden jig for folding metal mesh pads.

Figure 5 (a)-(c) displays the folding process utilizing the wooden jig. To begin, a length of metal mesh (~1.6 m) locates in the wooden jig and a C-clamp (labeled in Figures 4 & 5 as “Tension device”) secures one end. Once secured, the manufacturer folds the mesh, end over end, in the wooden jig. After each fold, the manufacturer compresses the folded length of mesh between two wooden blocks to ensure that the pad maintains its parallelism. The completed metal mesh roll has a width of 5.71 cm and a length of ~8.13 cm.

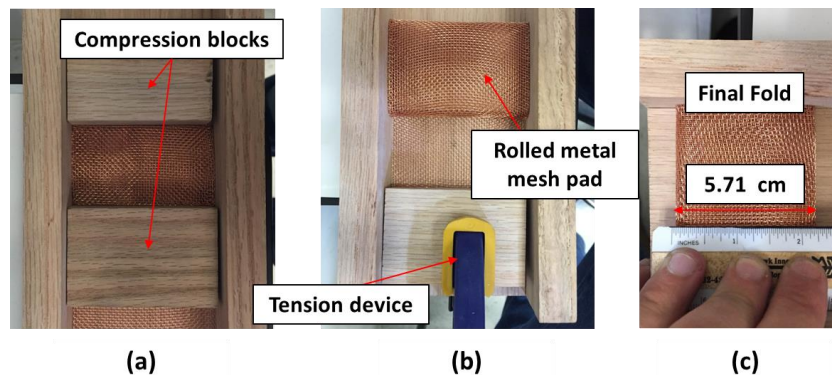


Figure 5. Folding process of a metal mesh pad in a dedicated wooden jig.

The next step in the forming process utilizes a machined jig and hydraulic press to compress the metal mesh rolls into the shape displayed in Figure 1. Figure 6 displays an exploded view of the metal mesh compression jig, consisting of four AISI 1020 steel pieces joined together by standard ¼” bolts. The roll of mesh locates in the cavity between the assembled pieces and compresses to the desired curvature and volume.

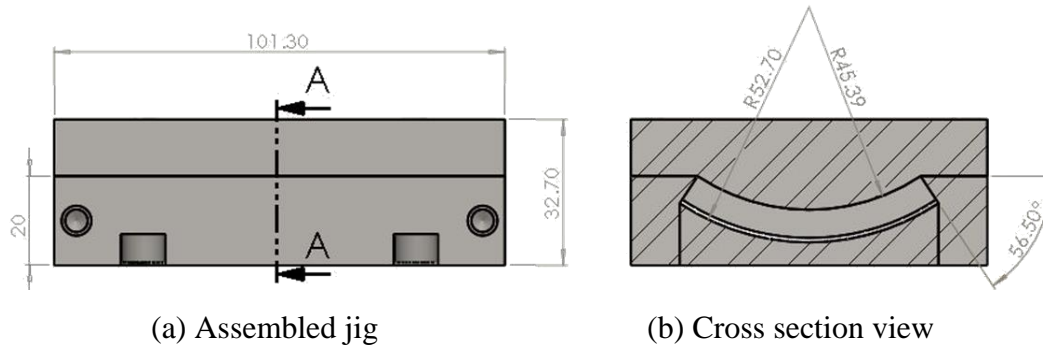


Figure 6. Schematic views of a metal jig for forming metal mesh pads. Dimensions in mm.

Figure 7 displays the metal mesh forming jig installed in a hydraulic press. The hydraulic press (piston area of 32.2 cm^2) applies a large load on the metal mesh roll equal to 68.7 kN ($W/A_{pad} = 15.9 \text{ MPa}$) for a period of ten seconds. Whenever a large load applies to the mesh, it forms to the desired shape, without noticeable spring-back. After the time elapses, the manufacturer removes the load and disassembles the metal jig to remove a formed metal mesh pad. Implementing the above process forms five metal mesh pads of nearly identical dimensions.

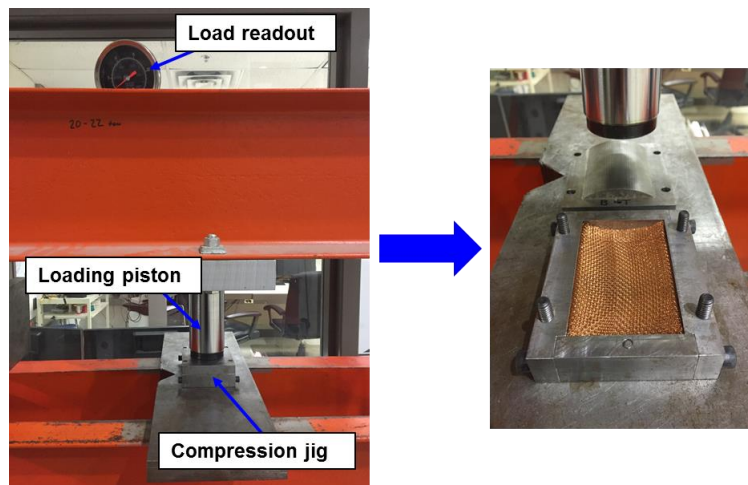


Figure 7. Compression of a metal mesh pad in a dedicated jig.

STATIC AND DYNAMIC FORCED PERFORMANCE OF FORMED METAL MESH PADS

Figure 8 displays a schematic isometric view and a cross section view of a test rig designed to measure the static and dynamic load performance of metal mesh pads. The test rig consists of two major components, a fixed base and a sliding assembly. The solid metal base, with a machined radius equal to the outer radius of the mesh pads ($R_1 = 52.7$ mm), affixes to a bedplate via four bolted connections. Four smooth Dowel pins (press fit to maintain rigidity) locate at the corners of the base and act as linear guides for the sliding assembly. The sliding assembly comprises of a curved piece with an outer radius equal to the mesh pads' inner radius ($R_2 = 45.34$ mm) connected to a flat plate and a rectangular piece of steel (labeled "Shaker block"). The shaker block connects the sliding assembly to an electromagnetic shaker (not pictured). The flat plate has a hole in each corner and four accompanying plastic bushings that allow free sliding over the smooth Dowel pins in the fixed base. Two additional holes at the centerline allow the flat plate to slide (without contacting) over threaded rods, attached to the fixed base. Two springs of known stiffness attach to the threaded rods and apply a desired preload to the metal mesh pad.

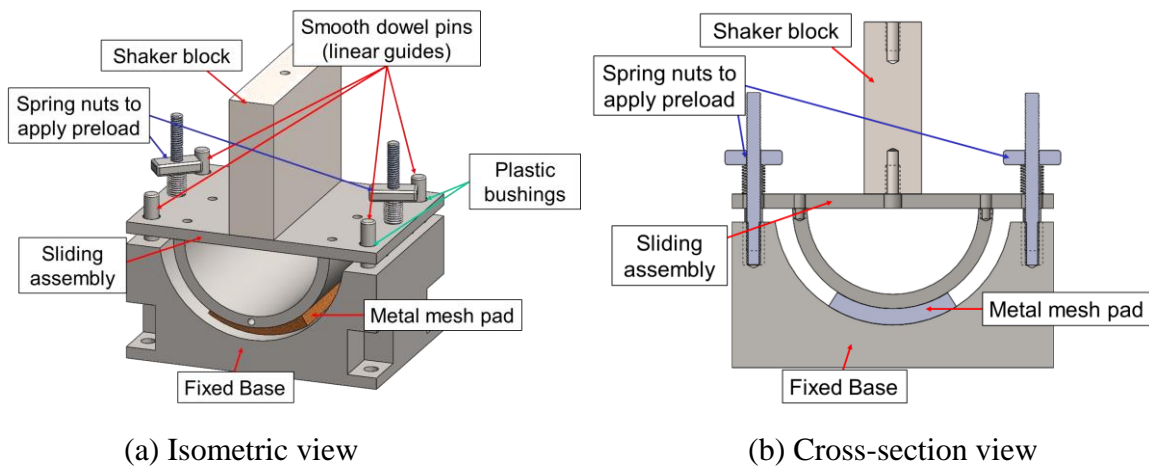


Figure 8. Schematic views of a test rig for loading a formed metal mesh pad.

STATIC LOAD MEASUREMENTS

After the compression process described in a previous section, the manufacturer originally measured the thickness of the metal mesh pads with digital calipers (this

process later proved to be inaccurate). Even after compressing the pads with a specific load of nearly 16 MPa in the hydraulic press, there is noticeable compression (~0.5 mm) when grasping the pad between the caliper teeth. This makes the determination of a pad thickness with traditional instruments (calipers, micrometers, etc.) difficult, likely inconsistent.

Figure 9(a) displays a formed metal mesh pad, indicating six locations for measuring the pad thickness, while Figure 9(b) displays an isometric view of a pad undergoing a single thickness measurement, taken at location 2. Notice that the thickness measurement is not a point measurement, but occurs along the entire length of the caliper teeth. In addition, a thickness measurement consists of compressing the pad between the caliper teeth until the pad acts as a rigid surface. Once the operator compresses the pad to take out the initial compliance, and it becomes hard to compress the pad further between the caliper teeth, the manufacturer records the thickness. This thickness is herein referred to as the pad compressed thickness.

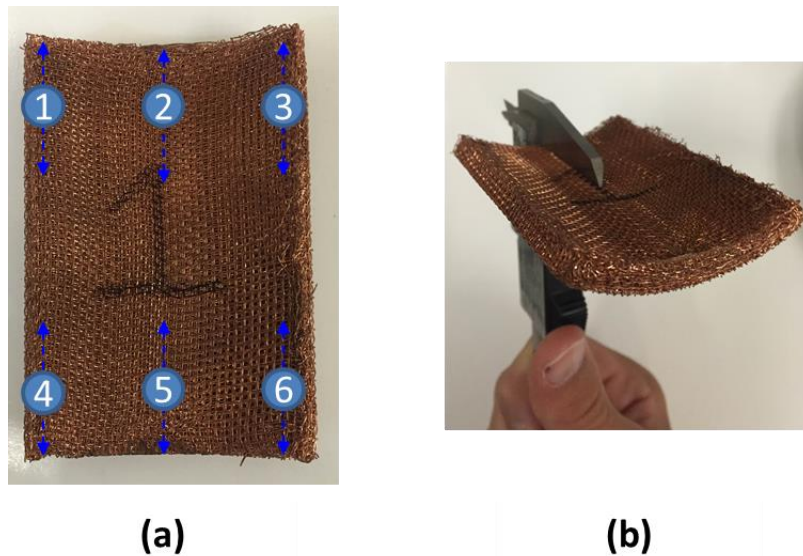


Figure 9. (a) Photograph of a metal mesh pad including measurement locations and (b) a photograph of a thickness measurement taken at location 2.

Three compressed thickness measurements at each of the six locations determine the thickness of each metal mesh pad and account for repeatability. Table 3 displays the measured thicknesses as well as the average pad thickness for each of the five metal mesh

pads. The thickness measurements displayed in Table 3 show that the five metal mesh pads have markedly similar center dimensions (locations 2 and 5), yet these thickness measurements introduce uncertainty and are only displayed as an indication of incorrect practice when measuring the pads' thickness.

Table 3. Pad compressed thicknesses (undetermined compressive loads applied). Thickness measurements in mm.

Metal Mesh Thickness at Locations Displayed in Figure 10 [mm]								
	1	2	3	4	5	6	Average	Deviation
Pad #1	6.49	6.90	6.71	6.5	6.94	6.71	6.71	0.45
Pad #2	6.64	7.00	6.68	6.55	7.03	6.7	6.77	0.48
Pad #3	6.65	7.03	6.67	6.64	7.01	6.65	6.78	0.38
Pad #4	6.54	7.02	6.71	6.48	6.99	6.71	6.74	0.54
Pad #5	6.71	7.01	6.74	6.65	6.99	6.75	6.81	0.36

The difficulty in measuring the pad thickness with conventional measurement instruments (calipers, micrometers, etc.) necessitates a new method. Figure 10 displays the metal mesh test rig from Figure 9 installed on the positioning table of a vertical mill. The mill chuck attaches to the sliding assembly via a strain gauge load cell, while two eddy current sensors locate on either side of the arcuate piece. The metal mesh pad sits between the fixed base and the arcuate piece attached to the sliding assembly.

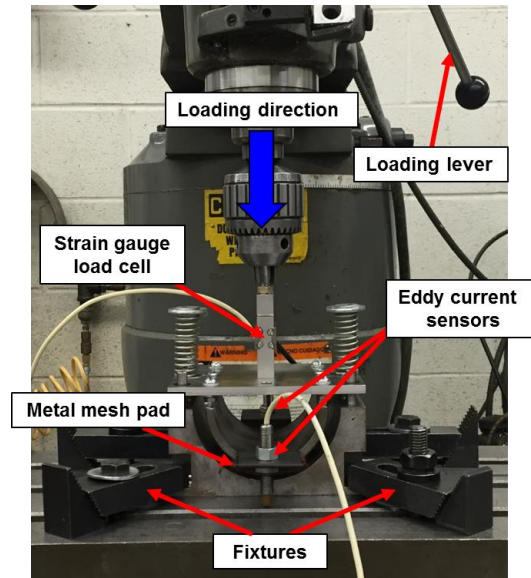


Figure 10. Metal mesh test rig installed in a vertical mill for static load testing.

The vertical mill pictured in Figure 10 provides a digital display (resolution ± 0.005 mm) for measuring the vertical movement of the sliding assembly affixed to the chuck. Prior to installing the metal mesh pad in the test rig (nothing between the fixed base and sliding assembly) the operator zeros the digital display at the location where the two curved surfaces are in solid contact and the load cell is undeflected (load cell must display less than 0.45 N of load), as shown in Figure 11. This null position provides a datum from which the operator can measure the thickness of a metal mesh pad, once installed in the rig.

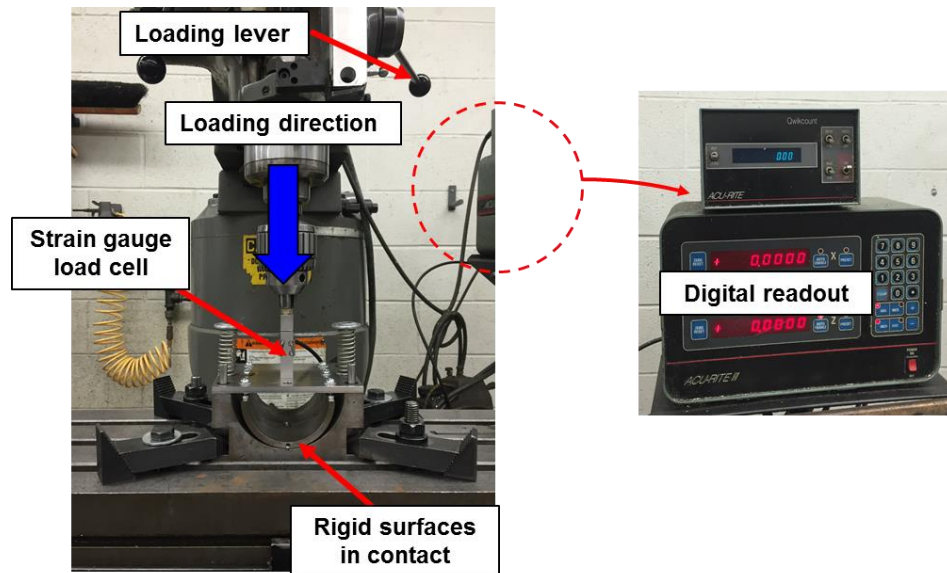


Figure 11. Obtaining a datum for thickness measurements with the metal mesh test rig installed in a vertical mill.

After installing a metal mesh pad in the test rig, the operator applies a load of 2.22 N (± 0.22 N) to the mesh pad and records the thickness of the pad from the digital display. This thickness measurement is referred to herein as the pad *first-touch* thickness. Table 4 displays the *first-touch* thicknesses for each of the five metal mesh pads. The results displayed in Table 5 show that four of the pads have not been compressed to the designed thickness of 7.36 mm; however, Pad #4 is 7.29 mm thick, slightly below the designed dimension. In addition, note that although their thickness is not the designed thickness (7.36 mm), pads 1, 2, 3 and 5 display similar thicknesses. In addition, the *first-touch* thicknesses in Table 4 are substantially different from those displayed in Table 3, showing that the compressed thickness measurement is both inaccurate and unnecessary.

Table 4. First-touch thicknesses of five manufactured metal mesh pads (applied load = 2.22 N).

	Metal Mesh Thickness [mm]					
	Trial 1	Trial 2	Trial 3	Trial 4	Trial 5	Average
Pad #1	7.59	7.59	7.59	7.59	7.59	7.59
Pad #2	7.54	7.54	7.54	7.54	7.54	7.54
Pad #3	7.61	7.61	7.61	7.61	7.61	7.61
Pad #4	7.29	7.29	7.29	7.29	7.29	7.29
Pad #5	7.60	7.60	7.60	7.60	7.60	7.60

With the test rig still installed in the vertical mill, a load and unload cycle up to ~0.9 kN (max $W/A_{pad} = 200$ kPa, 2 bar), recording data points every 50 μm , determines the static behavior of the metal mesh pads. Figure 12 displays the specific load W/A_{pad} (where $A_{pad} \sim 43.12 \text{ cm}^2$) versus deflection behavior of the five metal mesh pads. The results in Figure 12 closely resemble those from a previous TRC report [13], evidencing an initial region where small loads (less than 100 N, $W/A_{pad} = 17$ kPa) result in displacements as large as 0.75 mm, which is greater than 50% of the total measured displacements.

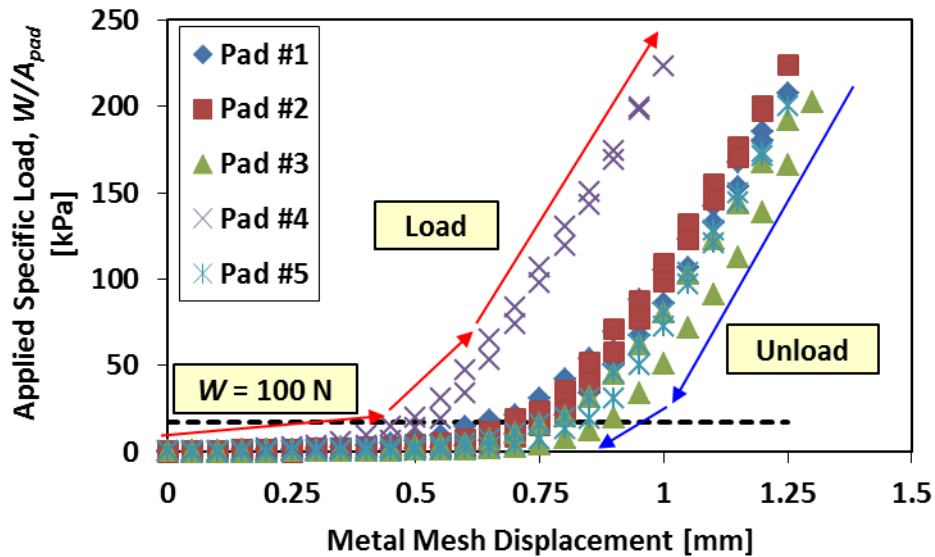


Figure 12. Specific load (W/A_{pad}) versus displacement for five metal mesh pads.

As in Ref. [13], an odd order polynomial models the pad reaction force $F(x)$ as a function of the mesh deflection (x). Presently,

$$F(x) = K_1x + K_2x^2 + K_3x^3 \quad (5)$$

is quite adequate to fit the test data with a good correlation coefficient ($R^2 \geq 0.99$). Figure 13 includes the third order polynomial curve fits and Table 5 lists the coefficients for the polynomials.

Table 5. Coefficients of polynomials fitting recorded deflection and load data.

Load F (N) vs displacement x (mm)				
$F(x) = K_1x + K_2x^2 + K_3x^3$				
Pad #	K_1 [N/mm]	K_2 [N/mm ²]	K_3 [N/mm ³]	R^2
1	14.55	-239.08	656.89	0.99
2	40.5	-446.37	848.4	0.99
3	86.98	-561.87	809.95	0.99
4	-211.24	601.07	606.02	0.99
5	194.04	-915.36	1063.6	0.99

The bearing structural stiffness K_{struct} is

$$K_{struct} = \frac{dF}{dx} = K_1 + 2K_2x + 3K_3x^2 \quad (6)$$

Figure 13 displays the derived static stiffness (K_{struct}) versus mesh displacement for five pads. The structural stiffness of a pad increases with the applied load, as more of the mesh layers come into contact. Four pads (1, 2, 3 & 5) display similar structural stiffnesses, with Pad 4 being markedly stiffer. For the range of applied loads (0-900 N), the maximum structural stiffness is ~ 2.9 MN/m.

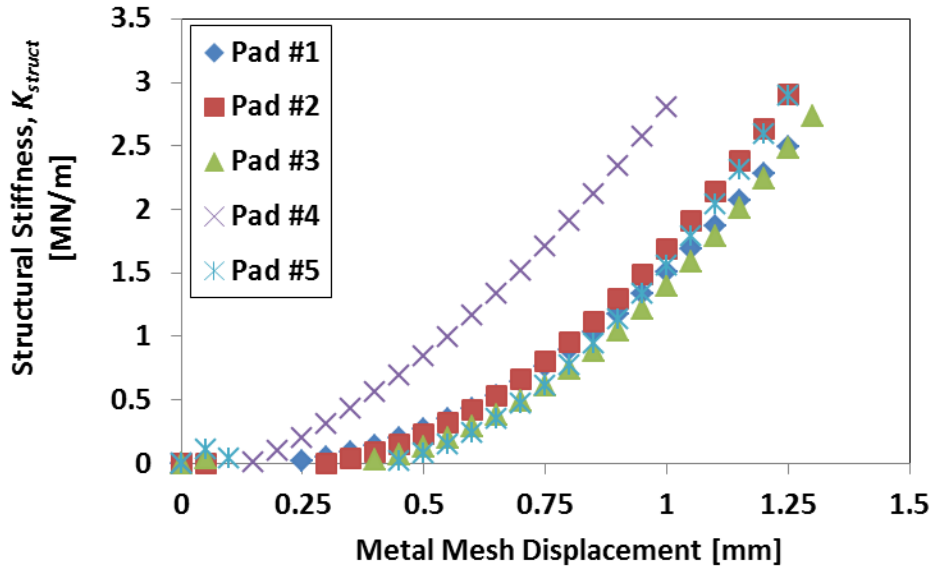


Figure 13. Metal mesh structural stiffness versus mesh displacement.

The static load measurements show that the pads behave similarly, with a maximum structural stiffness of ~ 2.9 MN/m; however, the magnitudes of the mesh displacements vary as much as 0.1 mm at the maximum applied load of ~ 0.9 kN (specific load of 205 kPa) from pad to pad.

The following section assesses the effects of the noted differences on the dynamic load performance of the mesh pads.

DYNAMIC TEST RIG, MODEL AND TEST RIG SHAKEDOWN

During airborne operation, the gas film and underspring structure (metal mesh) contribute to the stiffness and damping of a gas foil bearing. The air film and the mesh structure act as springs in series. Characterizing the dynamic performance of the individual mesh pads provides a metric for evaluating if the differences in thickness (shown in Table 5) do affect the performance of the assembled bearing.

Figure 14 displays a photograph of the metal mesh test rig assembled on a bedplate and with a support structure designed for dynamic load testing. An electromagnetic shaker (max load ~ 100 N), flexibly mounted for ease of alignment, connects to the sliding assembly via a dynamic load cell and threaded connection. Note that the stiff connection between the shaker armature and the shaker block couples the shaker to the

test element. In addition to the dynamic load cell, an accelerometer and two eddy current sensors measure the absolute acceleration and absolute displacements of the sliding assembly, respectively. Two compression springs ($K_S = K_1 + K_2 = 6.16 \text{ kN/m}$), cold-welded to the sliding assembly, provide a means of applying a desired mechanical preload (static load) to a test pad.

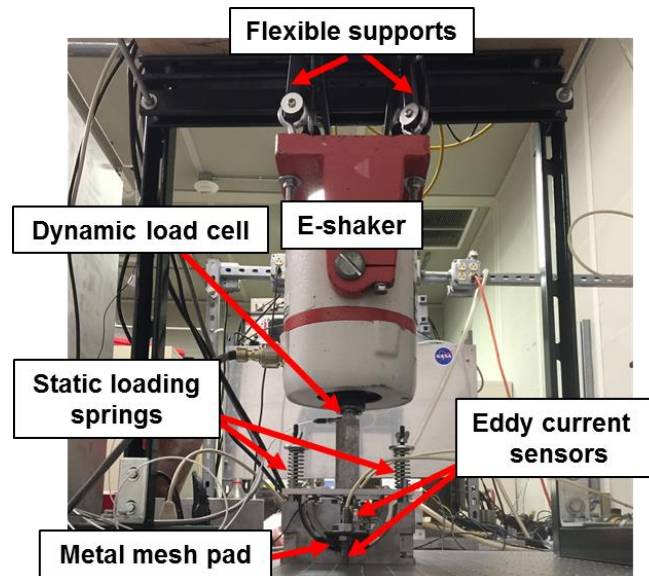


Figure 14. Metal mesh test rig assembled for dynamic load measurements.

Figure 15 displays a front view of the test rig from Figure 14 as well as a corresponding single degree of freedom (SDOF) model for the system. The simple SDOF model considers the sliding assembly as rigid body ($M = 3.18 \text{ kg}$) excited by an electromagnetic shaker with force $F(t)$. In the following figure, the subscript S denotes “structural” whereas the subscript MM refers to “metal mesh”. When the shaker aligns with the fixed base, there is no sliding contact between the plastic bushings and their Dowel pins. Thus, the contact between the pins is considered to have a negligible contribution to the system stiffness and damping. When the compression springs on the sliding assembly apply a preload to the mesh pad, a structural stiffness from the springs

acting in parallel ($K_S = 6.16 \text{ kN/m}$) appears in the model (displayed on Figure 15)¹. Note that the simple model considers the metal mesh pad as a linear spring and viscous damper as in Refs. [2,5].

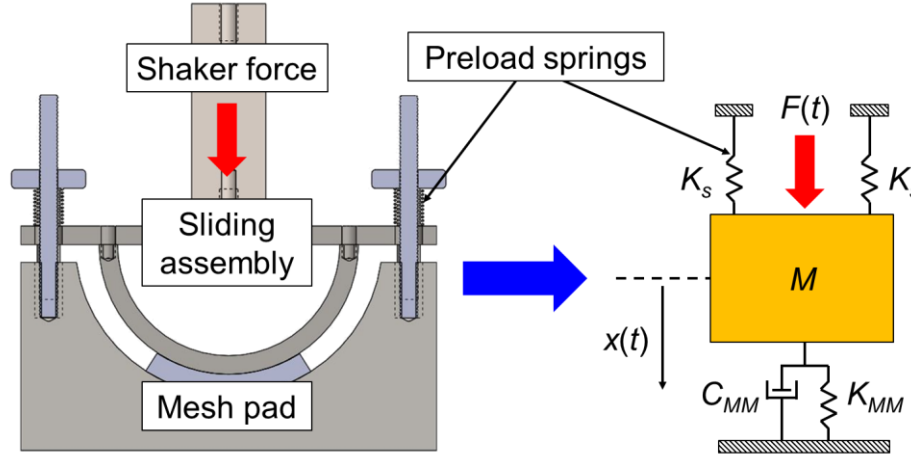


Figure 15. Schematic view of the metal mesh test rig and corresponding single degree of freedom model.

The equation of motion (EOM) for the single degree of freedom system displayed in Figure 15 is

$$M\ddot{x} + C_{MM}\dot{x} + (K_{MM} + 2K_S)x = F(t) \quad (7)$$

where M is the mass of the sliding assembly ($\sim 3.18 \text{ kg}$), C_{MM} is the metal mesh damping and $K_{eq} = K_{MM} + 2K_S$ is the equivalent stiffness for the test rig and metal mesh pad.

Consider a periodic force $F(t)$ and ensuing periodic displacement (with the same frequency)

$$F(t) = \bar{F}e^{i\omega t} \rightarrow x(t) = \bar{X}e^{i\omega t} \quad (8)$$

where $i = \sqrt{-1}$, ω is the excitation frequency and t is time. Substituting the definitions in Eq. (8) into Eq. (7), gives the EOM in the frequency domain as

$$-M\omega^2 + i\omega C_{MM} + K_{eq} = \frac{\bar{F}}{\bar{X}} \quad (9)$$

¹ The compression spring stiffness (K_S) is less than 2% of the smallest identified dynamic stiffness of the metal mesh pads (shown in Figure ...).

The real and imaginary parts of Eq. (9) represent the dynamic stiffness and damping of the compressed metal mesh pad as well as any contributions from the compression springs.

$$\begin{aligned}
 -M\omega^2 + K_{eq} &\leftarrow \operatorname{Re}\left(\frac{\bar{F}}{\bar{X}}\right) \\
 \omega C_{MM} &\leftarrow \operatorname{Im}\left(\frac{\bar{F}}{\bar{X}}\right)
 \end{aligned}
 \tag{10}$$

Before conducting dynamic load tests, an impact test of the sliding assembly (pictured in Figure 16) determines its vibration characteristics. A commercial DAQ records the corresponding acceleration from a single axis accelerometer (10.6 mV/g) at a frequency of $f_s = 10$ k-samples/s.

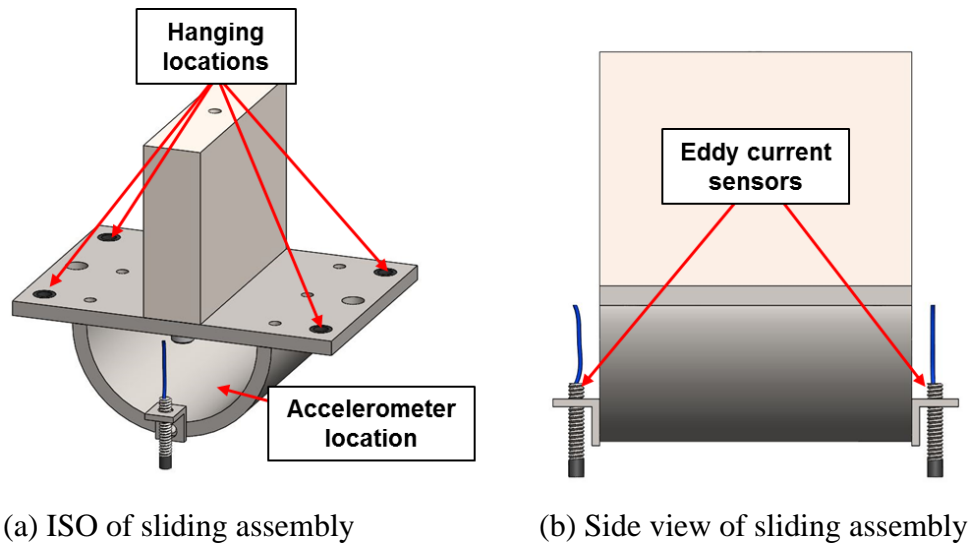


Figure 16. Schematic views of the sliding assembly for free-free impact tests.

Figure 17 displays the time domain signal and corresponding frequency domain content. Note that the frequency domain plot (Figure 17 (b)) is an average of ten impacts in the frequency domain. Results show that the sliding assembly has a first natural frequency of ~ 20 Hz. The FFT also reveals structural elastic resonances at ~ 680 Hz and 900 Hz. However, the excitation range for the dynamic tests reported herein is 0-300 Hz, such that the higher modes of the sliding assembly are of no consequence.

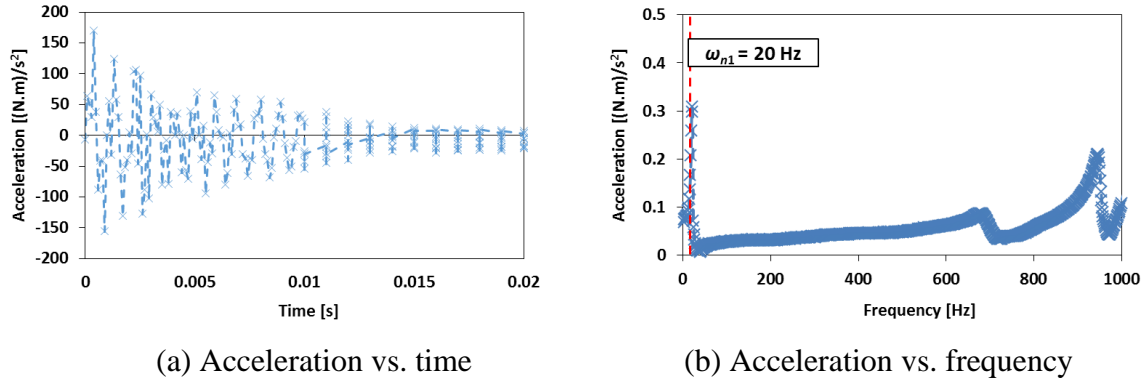


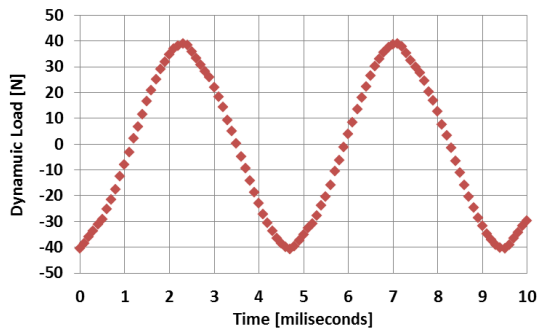
Figure 17. (a) Measurements of sliding assembly vibration versus time and (b) corresponding frequency spectrum.

The electromagnetic shaker and amplifier for the dynamic testing herein are capable of delivering a maximum load of ~ 100 N (22 lbf). The goal of the current tests is to compare against each other the pads dynamic load performance as well as to evaluate the dynamic structural characteristics of the metal mesh pads for various motion amplitude and preload. As such, an iterative process determines that for a frequency range from 0-300 Hz the shaker can deliver up to $30 \mu\text{m}$ peak-peak displacements under four chosen static preloads ($W \sim 30, 60, 90$ and 120 N)² applied by the preloading springs (K_s).

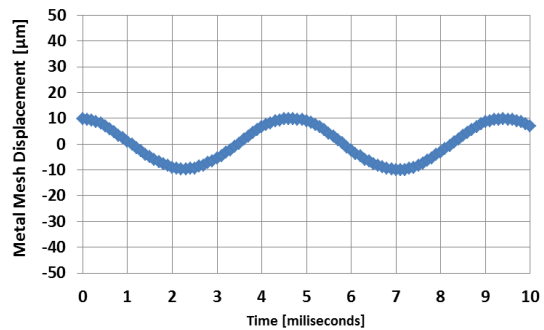
Single frequency excitations in 30 Hz increments characterize the dynamic performance of the individual metal mesh pads (no noise from electrical frequencies observed during testing). The dynamic load applied to the sliding assembly as well as the absolute acceleration and displacements of the sliding assembly are recorded with a commercial DAQ at a sampling frequency of $f_s = 10$ k-samples/s. An in-house LabView® virtual instrument (VI) allows the operator to tune the amplitude and frequency of the output waveform until the desired motion amplitude occurs. Once the desired motion amplitude is achieved, ten sets of data are recorded for one second each (total of 10 seconds of data per frequency).

² $W/A_{pad} = 7, 14, 21$ and 28 kPa, respectively.

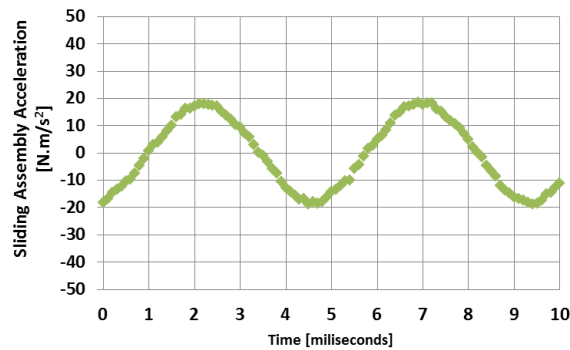
Figure 18 displays two full periods of the measured sliding assembly force (F), displacement (x), and acceleration (\ddot{x}) versus time for Pad #5 conducted at an excitation frequency of 210 Hz, a static preload $W = 60$ N (specific load of 14 kPa), and a motion amplitude of $20 \mu\text{m}$ peak-peak. The measured force, displacement and acceleration signals are smooth; however, at lower excitation frequency (less than 150 Hz), corresponding to small dynamic forces (less than 20 N peak-peak), the signals are more erratic.



(a) Dynamic Force, $F(t)$



(b) Displacement, $x(t)$



(c) Acceleration, $\ddot{x}(t)$

Figure 18. Measured (a) force (b) displacement and (c) acceleration versus time for Pad #5. $\omega_e = 210$ Hz, $W/A_{pad} = 14$ kPa.

To analyze the dynamic data, a Fourier series, utilizing a single Fourier coefficient at the fundamental (excitation) frequency, approximates the measured displacement, force and acceleration, respectively. The model in Eq. (7) assumes no relative motion between the sliding assembly and the support structure (i.e. $\ddot{x} \approx -\bar{X} \omega^2 e^{i\omega t}$). Figure 19 displays the

measured and approximate accelerations (average of 10 trials per frequency) of the sliding assembly versus excitation frequency for Pad #5 with a preload $W = 60$ N and a displacement amplitude of $20 \mu\text{m}$ peak-peak. The measurements show less than 7% difference ($100 \cdot \left[\frac{\bar{A} - \omega^2 \bar{X}}{\bar{A}} \right]$) between the measured acceleration and derived accelerations above 30 Hz, validating the assumption of no relative motion.

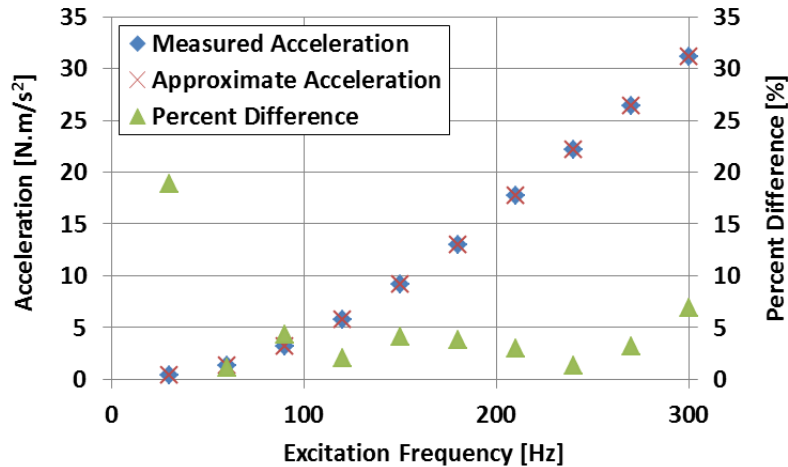
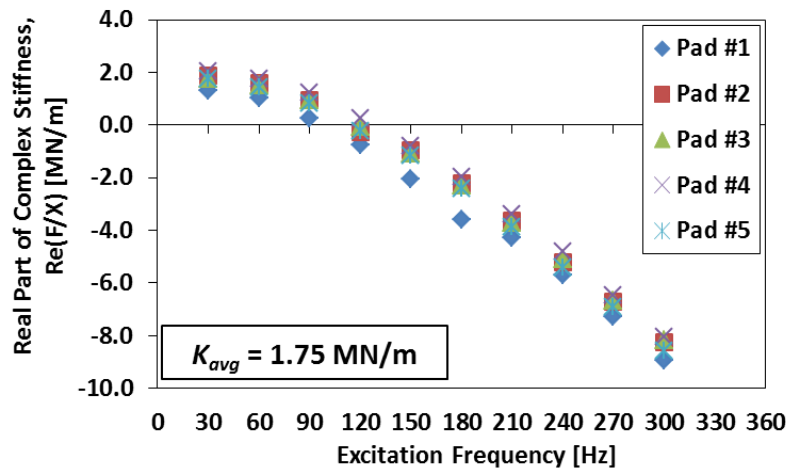


Figure 19. Comparison of measured and derived amplitudes of acceleration versus frequency for Pad #5. $W = 60$ N, $|\bar{X}| = 10 \mu\text{m}$.

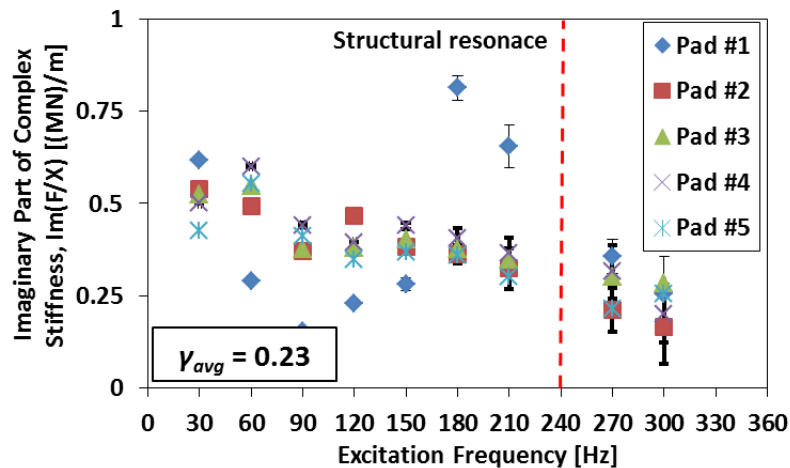
COMPARISON OF DYNAMIC PERFORMANCE FOR (FIVE) METAL MESH PADS

The following plots compare the dynamic performance (stiffness and material damping) of five formed metal mesh pads subjected to a preload of $W = 60$ N ($W/A_{pad} = 14$ kPa) and a displacement amplitude of $|\bar{X}| = 10 \mu\text{m}$. Figure 18 displays the real and imaginary parts of the complex stiffness (\bar{F}/\bar{X}) versus frequency. Both plots include error bars on the measurements, calculated with a standard t -distribution and a 95% confidence interval [16] (Appendix A gives details on the uncertainty analysis). Note that the imaginary parts of the complex stiffness (\bar{F}/\bar{X}) increase at ~ 240 Hz due to a structural resonance of the preload springs (each of the following plots highlights this frequency).

The real part of the complex stiffness in Figure 20 (a) is representative of a SDOF system with a linear spring, i.e. $\text{Re}(\bar{F} / \bar{X}) \rightarrow -M\omega^2 + K_{eq}$. Notice that the variability in the measurements is small enough that the error bars do not extend outside of the data markers. The imaginary part of the complex stiffness, displayed in Figure 20(b), shows a general decrease with excitation frequency and indicates almost zero variability (as indicated by the error bars) for excitation frequency less than 180 Hz. Most importantly, notice that the real part of the complex stiffnesses follow the same qualitative trends for the five pads and are nearly equal in magnitude. The same is true of the imaginary parts.



(a) Real part of complex stiffnesses (\bar{F} / \bar{X})



(b) Imaginary part of complex stiffnesses (\bar{F} / \bar{X})

Figure 20. (a) Real part and (b) imaginary part of the complex stiffness versus excitation frequency for five metal mesh pads. $W/A_{pad} = 14$ kPa, $|X| = 10$ μm .

From the simple SDOF model described in a previous section, Eq. (10) shows that the real part of the complex stiffness determines the equivalent mass and stiffness of the system, i.e. $\text{Re}(\bar{F} / \bar{X}) \rightarrow -M\omega^2 + K_{eq}$. A linear curve fit of the real part of the transfer function versus ω^2 renders K_{eq} , M_{eq} . Table 6 displays the identified metal mesh stiffness (K_{MM}), equivalent mass (M_{eq}), derived natural frequency and the R^2 (goodness of fit) value associated with the linear curve fit. Recall that the mass of the sliding assembly is 3.18 kg (as measured with a digital scale, resolution of ± 0.02 kg). Note that the predicted natural frequency corresponds to the locations where $\text{Re}(\bar{F} / \bar{X}) \rightarrow 0$, as shown in Figure 20(a).

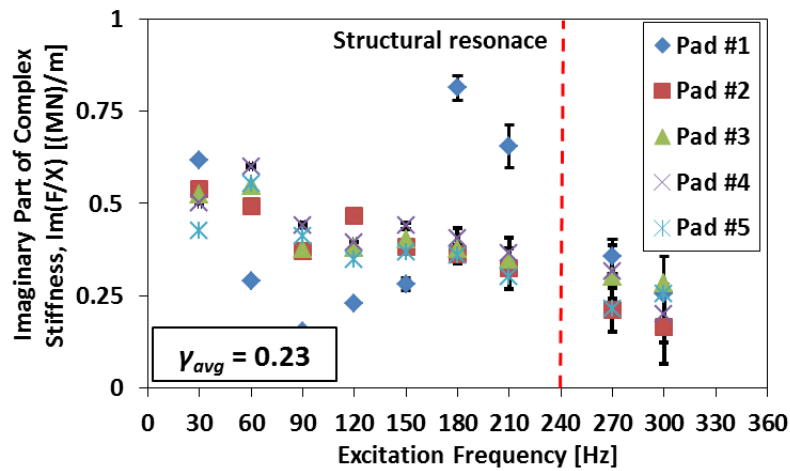
Table 6. Metal mesh pad stiffness for five manufactured metal mesh pads. Dynamic motion amplitude of 20 μm peak-peak and ~ 60 N ($W/A_{pad} = 14$ kPa) of preload. Frequency range $\omega_e = 0\text{-}300$ Hz.

	Pad #1	Pad #2	Pad #3	Pad #4	Pad #5
Linear stiffness coefficient, K_{MM} [MN/m]	0.96	1.70	1.64	1.96	1.59
Excited Mass, M [kg]	2.91	2.93	2.89	2.92	2.98
Natural Frequency, $\sqrt{K_{MM}/M}$ [Hz]	92	122	121	131	117
R^2 Value [-]	0.986	0.994	0.995	0.996	0.995

The imaginary part of the complex stiffness is clearly not representative of a linear viscous damping, i.e. $\text{Im}(\bar{F} / \bar{X}) \neq C\omega$. This result is consistent with published measurements in the literature on small diameter metal mesh bearings [5,6] as well as metal mesh bearing dampers [3,4], that show a decrease in the imaginary part of the transfer function with an increase in frequency. San Andrés *et al.* [5] state that a material loss factor best models the damping in the metal mesh structure, being structural (hysteretic) in nature. A loss factor for the metal mesh pad is defined as

$$\gamma = \frac{\text{Im}(\bar{F} / \bar{X})}{K_{MM}} \quad (11)$$

Figure 21 displays the loss factor versus excitation frequency for the five manufactured metal mesh pads. Pads 2-5 show similar γ , starting at ~ 0.3 at a low frequency and decreasing with increasing excitation frequency. The large loss factor for Pad #1 is likely due to its artificially low stiffness coefficient (as displayed later). For a preload of $W = 60$ N (14 kPa specific load), the pads shows a moderate size loss factor (less than 0.5). Earlier, San Andrés *et al.* [5] report a loss factor as high as 0.7 for an assembled small diameter (42 mm) MMFB. Note that the material loss factor should be relatively constant over the frequency excitation range. The table in Figure 21 shows that the variability in the loss factors (calculated with a standard Kline-McClintock and a 95% confidence interval as seen in Appendix A) is small (± 0.05), except for Pad #1, showing that the data for Pad #1 is likely in error.



Pad #	1	2	3	4	5
Average loss factor, $\gamma = \text{Im}(\bar{F}/\bar{X})/K_{MM}$	0.43 (± 0.23)	0.22 (± 0.05)	0.24 (± 0.05)	0.20 (± 0.04)	0.24 (± 0.05)

Figure 21. Material loss factor versus excitation frequency for five manufactured metal mesh pads. $W = 60$ N, $|X| = 10 \mu\text{m}$.

The data in Table 7 and the loss factors displayed in Figure 21 shows that Pads 2-5 have similar dynamic properties, while Pad #1 has a markedly lower stiffness and larger

$\text{Im}(\bar{F}/\bar{X})$, resulting in a larger γ . This result is not expected, since the load versus deflection data, displayed in Figure 12, shows the pads to have similar static stiffnesses.

At first glance, it appears a mistake was made during the dynamic testing of Pad #1. However, the tests with Pad 1 were repeated on three separate occasions, determining nearly identical results. As such, there must be a reason for the difference in the dynamic behavior displayed in Table 6 and Figure 19. Figure 22 portrays Pad #1 installed in the metal mesh test rig and preloaded with a load of $W = 90 \text{ N}$ ($W/A_{pad} = 21 \text{ kPa}$). The photograph shows that even at the second largest preload, the sliding assembly does not contact the pad over its full area, leading to a smaller loading area and reduced stiffness.

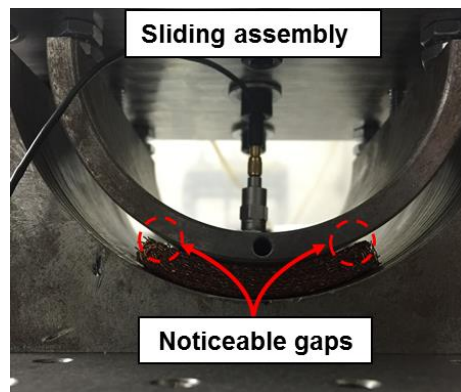


Figure 22. Photograph of Pad #1 installed in the metal mesh test rig for dynamic testing and with an applied preload of $W/A_{pad} = 21 \text{ kPa}$.

The photograph in Figure 22 indicates that the pad curvature differs from the designed dimension. Updates to the test rig will include the ability to vary the loading area to ascertain its effect on a metal mesh pad dynamic load performance.

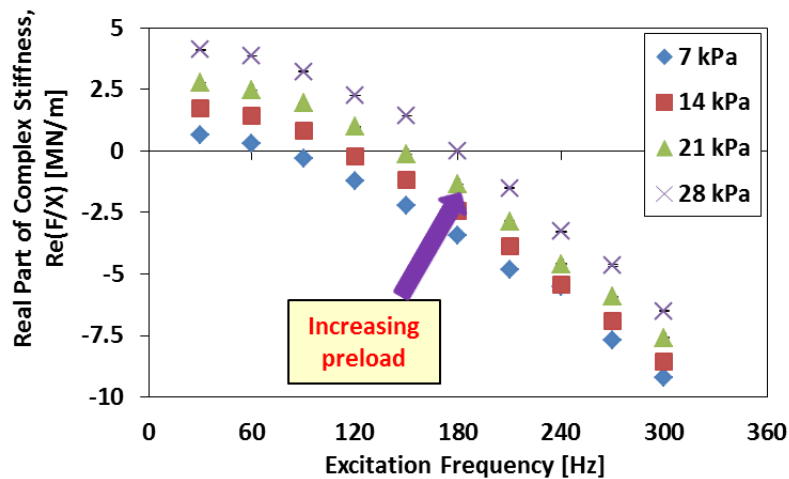
DYNAMIC FORCE RESPONSE TO VARIOUS MOTION AMPLITUDES AND PRELOADS

The results in Figure 20 show that the dynamic load performance of the five manufactured pads follow the same qualitative trends with excitation frequency. Extracted K_{MM} and γ are nearly identical in magnitude (with the exception of Pad #1). Based on this finding, the next section examines the effects of increasing preload ($W/A_{pad} = 7, 14, 21, \text{ and } 28 \text{ kPa}$) and dynamic motion amplitude (10, 20, and 30 μm peak-

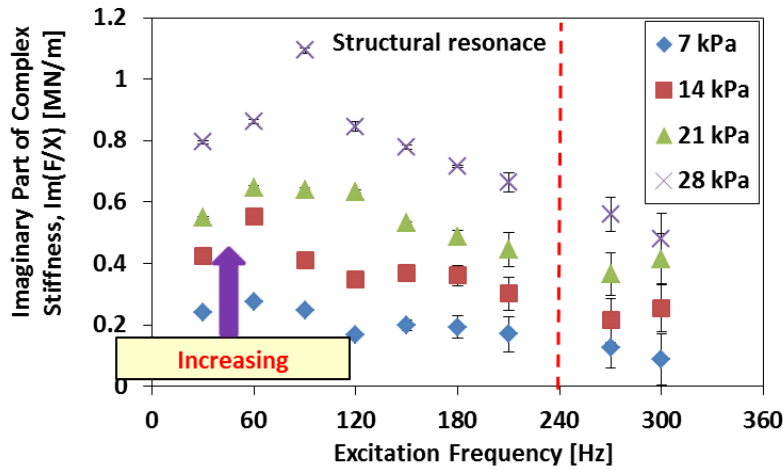
peak) on the dynamic force characteristics (stiffness and material loss factor) of Pad #5 alone, assuming the results can be extended to the other pads. As before, single frequency excitations in 30 Hz increments from 30-300 Hz characterize the dynamic characteristics of the metal mesh pad. In addition, the sampling frequency remains unchanged ($f_s = 10$ k-samples/s) and, to account for variability, ten tests are recorded per excitation frequency.

Figure 23 displays the real and imaginary parts of the complex stiffnesses versus excitation frequency for an increasing preload and a motion amplitude of 20 μm peak-peak on Pad #5. The results in Figure 23 show that both the real and imaginary parts of the complex stiffnesses increase with mechanical preload. As with the previous measurements (Figure 19), the variability in the real part of the dynamic stiffness (displayed as error bars for a 95% confidence interval) is small enough that the error bars do not extend past the data markers. The variability in the imaginary part of the complex stiffness is small for low frequency (less than 180 Hz) and grows with increasing frequency.

Alkhateeb [3] also shows that the real and imaginary parts of the complex stiffness (\bar{F}/\bar{X}) of wire mesh dampers increases with mechanical preload, indicating that the trend is common to metal mesh structures. As with the complex stiffnesses for the five metal mesh pads, shown in Figure 20, $\text{Re}(\bar{F}/\bar{X}) \rightarrow -M\omega^2 + K_{eq}$. The imaginary part $\text{Im}(\bar{F}/\bar{X})$ generally decreases with an increase in excitation frequency.



(a) Real part of complex stiffness (\bar{F}/\bar{X})



(b) Imaginary part of complex stiffness (\bar{F} / \bar{X})

Figure 23. (a) Real part and (b) imaginary part of the complex stiffness versus excitation frequency for Pad #5 and increasing preload. $|X| = 10 \mu\text{m}$.

Figure 24 displays the identified metal mesh stiffness coefficient (K_{MM}) versus pad preload as well as a linear curve fit and a corresponding R^2 magnitude. In addition, Figure 23 displays the derived static stiffness ($K_{struct} = \partial F / \partial x$) for Pad #5 for the applied loads 30-120 N. The results in Figure 24, show that the metal mesh dynamic stiffness increases linearly with the applied preload from 30-120 N (7 – 28 kPa). In addition, note that the stiffness increases by a factor of 10 even though the force shows a small increase (30-120 N). The pad dynamic stiffness (K_{MM}) is nearly equal to the static stiffness (K_{struct}) for small loads. As the applied load increases, so does the ratio between the extracted dynamic and structural stiffnesses K_{MM} / K_{struct} . The reason for this difference has yet to be determined.

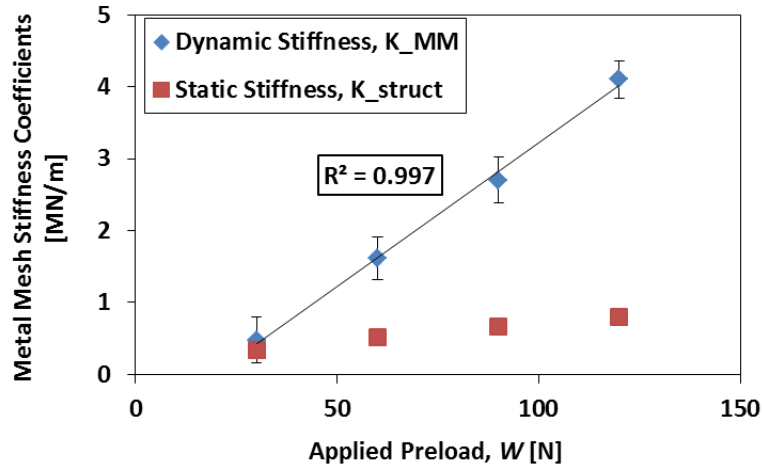
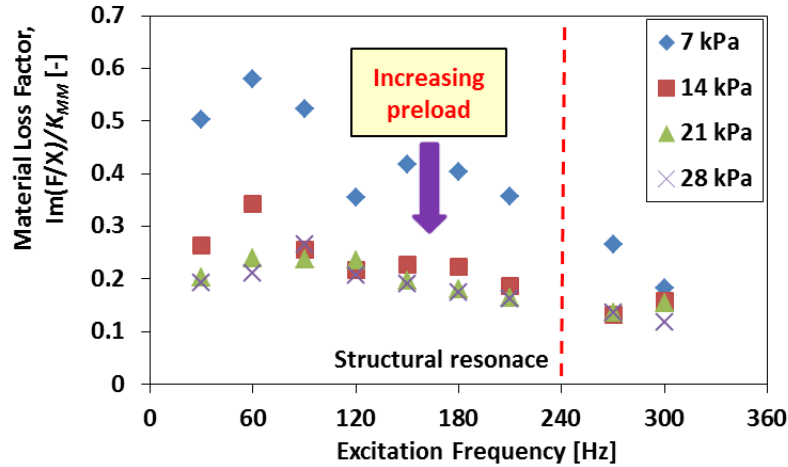


Figure 24. Identified MM Pad #5 stiffness coefficients versus applied preload. Results obtained for single frequency excitation from 30-300 Hz and a motion amplitude of $|X| = 10 \mu\text{m}$.

Figure 25 displays the estimated material loss factor (γ) versus excitation frequency for Pad #5 under an increasing preload. The results in Figure 25 show that γ is largest for the smallest preload ($W = 30 \text{ N}$), but with the largest associated uncertainty (± 0.30). The large uncertainty suggests that there is either a large variability in the real or the imaginary parts of the complex stiffness for the smallest preload. For the other three preloads, γ decreases with preload and has a small uncertainty (± 0.02 - 0.05). Alkhateeb [3], shows that the damping in metal mesh dampers increases with both axial compression and radial interference (i.e. preload).



W / A_{pad} [kPa]	7	14	21	28
Average loss factor, $\gamma = \text{Im}(\bar{F}/\bar{X})/K_{MM}$	0.41 (± 0.3)	0.24 (± 0.05)	0.21 (± 0.03)	0.18 (± 0.02)

Figure 25. Loss factor for Pad #5 versus excitation frequency for increasing preloads. $|X| = 10 \mu\text{m}$.

In addition to mechanical preload, the literature shows that motion amplitude has a significant effect on the dynamic performance of metal mesh bearings and dampers [3,5]. Figure 26 displays the metal mesh dynamic stiffness coefficient for Pad #5 extracted from $\text{Re}(\bar{F}/\bar{X})$ versus excitation frequency for Pad #5 subjected to three motion amplitudes (10, 20, and 30 μm peak-peak). Note that the pad preload is 60 N ($W/A_{pad} = 14$ kPa). In comparison to results from increasing the pad preload, the metal mesh dynamic stiffness decreases linearly with the amplitude of motion, nearly halving in magnitude over the limited range of tested amplitudes. Tests by San Andrés and Chirathadam [5] on a small metal mesh bearing (ID = 45 mm) show a similar trend.

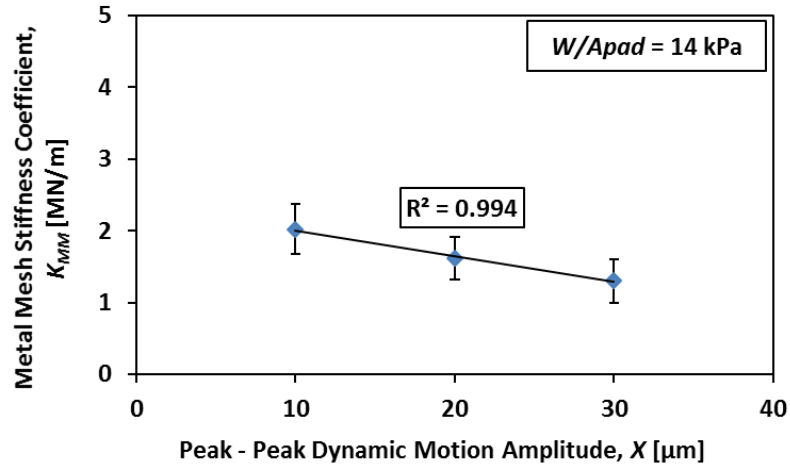
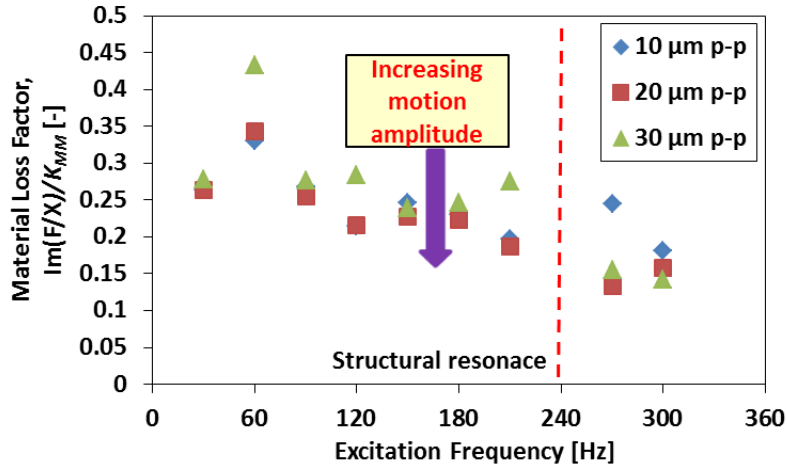


Figure 26. Metal mesh stiffness coefficient versus dynamic motion amplitude for Pad #5. $W/A_{pad} = 14$ kPa.

Figure 27 displays the material loss factor (γ) for Pad #5 versus excitation frequency derived from tests with three motion amplitudes and under a constant pad preload $W = 60$ N ($W/A_{pad} = 14$ kPa). γ remains relatively constant with an increasing motion amplitude. The plot neglects data at data at 240 Hz due to a structural resonance of the load springs.



Peak-peak Amplitude [μm]	10	20	30
Average loss factor, $\gamma = \text{Im}(\bar{F}/\bar{X})/K_{MM}$	0.26 (± 0.05)	0.24 (± 0.05)	0.30 (± 0.07)

Figure 27. Material loss factor versus excitation frequency for Pad #5 and increasing dynamic motion amplitudes. $W = 60$ N.

ASSEMBLY OF THE LARGE METAL MESH BEARING AND FUTURE WORK

The static and dynamic load measurements presented herein are for single pads, to determine the similarity, or differences amongst them. Although the material loss factor for the individual pads is small (less than 0.5), the trends and magnitudes displayed herein may not hold for the assembled bearing due to interactions between the pads themselves. The bearing also has a larger loading area $\sim 2.5A_{pad}$.

Figure 28 displays a photograph of the large diameter metal mesh bearing with the five manufactured pads and a stainless steel top foil (thickness = 254 μm). Table 1 is also reproduced below for convenience.

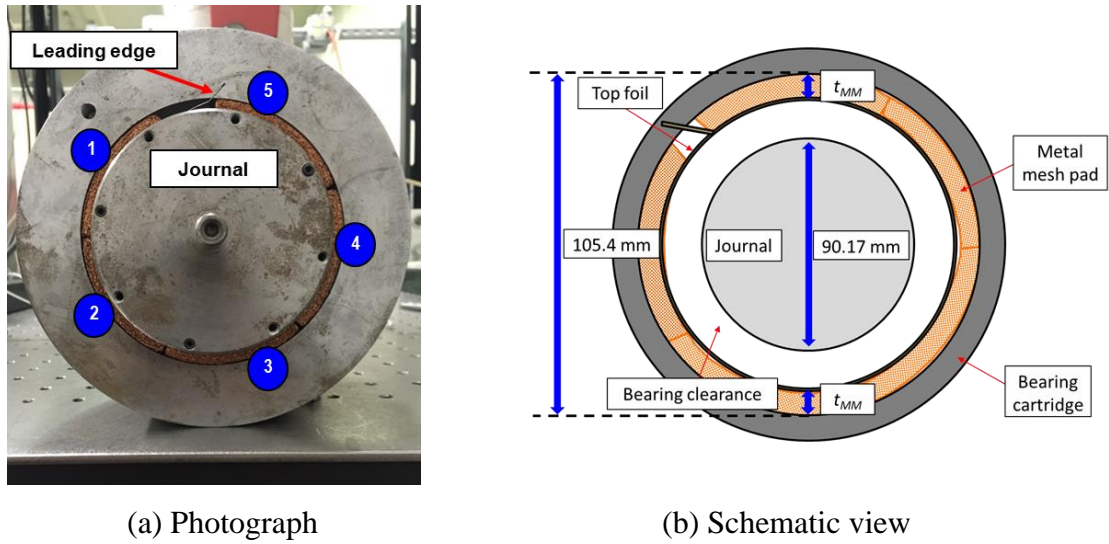


Figure 28. A (a) photograph and (b) a schematic view of an assembled metal mesh foil bearing with five metal mesh pads ($t_{MM} = 7.36$ mm).

Table 1. Bearing cartridge and rotor dimensions.

Parameter	Magnitude	Unit
Rotor mass, M_R	3	kg
Diameter, $D_{o,R}$	90.17	mm
Length, L_R	101.6	mm
Bearing cartridge mass, M_C	6.75	kg
Outer diameter, $D_{o,C}$	166.6	mm
Inner diameter, $D_{i,C}$	105.4	mm
Axial Length, L_C	81.3	mm
Pad axial length, L_{MM}	81.3	mm
Top Foil Material	316 SS	-
Top foil thickness, t_{tf}	0.254	mm
Length, L_{tf}	327	mm
Elastic modulus, E_{tf}	214	GPa

With the bearing assembled, next steps plan to test and characterize the bearing structural coefficients as well as its performance with respect to minimum film thickness, startup and operational drag torque, bearing temperature rise, and bearing load capacity. As mentioned at the outset of the technical report, a radial bearing test rig exists in the lab, making use of a 20 krpm (1.5 HP) router motor.

Unfortunately, tests determined that the router motor does not have the required torque or a speed controller to maintain a steady speed while spinning a journal inside of the large MMFB. To remedy this problem, Figure 29 displays a purchased water-cooled industrial router motor (3 HP, 40 krpm, 380 VAC) with a dedicated variable frequency drive (total price ~\$9,000). The motor will service both radial and thrust MMFB test rigs.

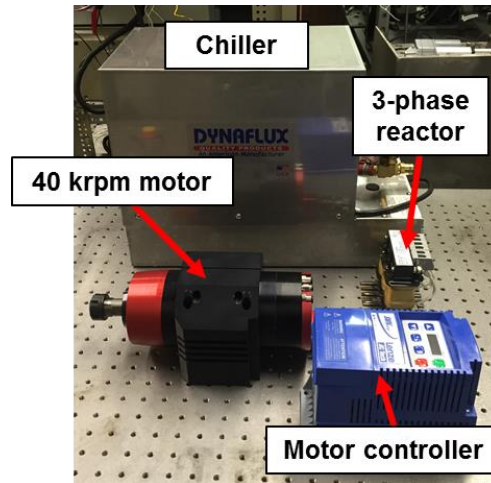


Figure 29. Photograph of a purchased 40 krpm, 3 HP motor, controller and dedicated chiller.

Future work intends to design and build two test rigs for the evaluation of radial and thrust foil bearings. The radial bearing rig involves a simple redesign or retrofitting of an existing rig, while the thrust bearing test rig necessitates a thorough design process and vetting, due to its complex nature.

Figure 30 displays a schematic view of the proposed foil thrust bearing test rig. The vertical design mimics the design of a similar rig from the Universite de Poitiers [17,18]. The proposed rig allows for the static and dynamic load characterization of thrust foil bearings. A hydrostatic plenum applies a downward load on a non-rotating loading shaft that secures the test thrust bearing. This loading shaft, that fits through an aerostatic bushing, which acts as a linear guide to control the position of the shaft and allow it to oscillate without friction for dynamic load testing.

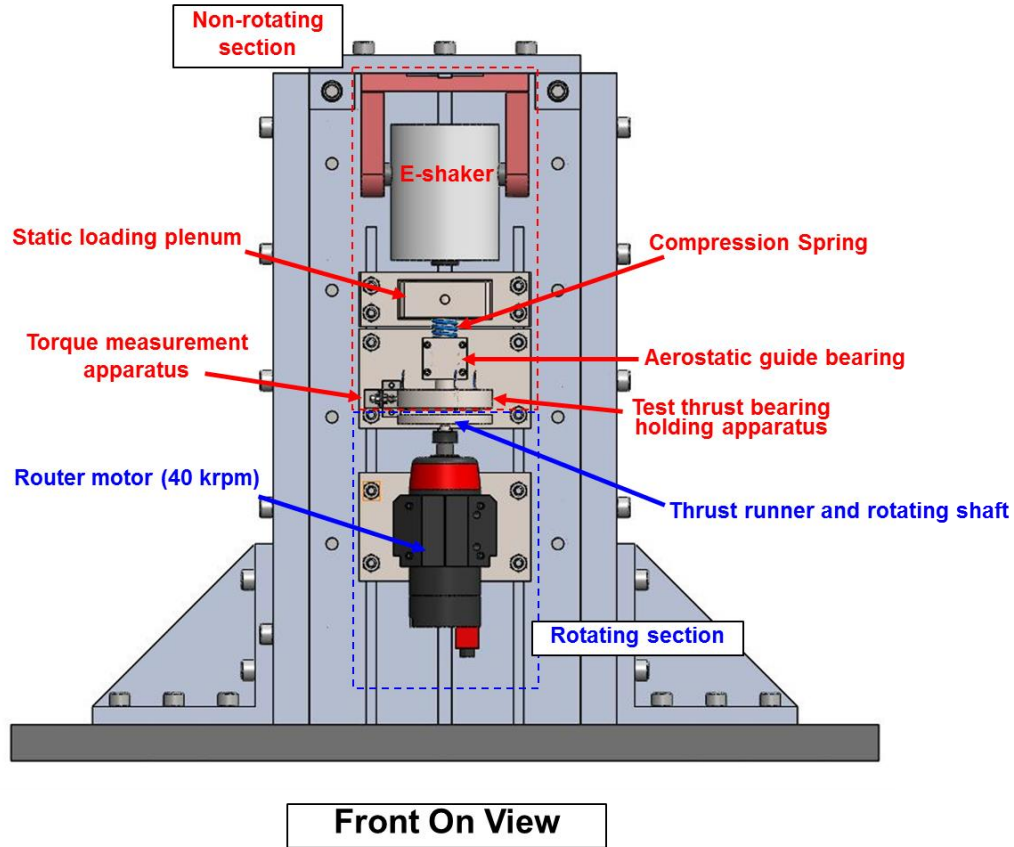
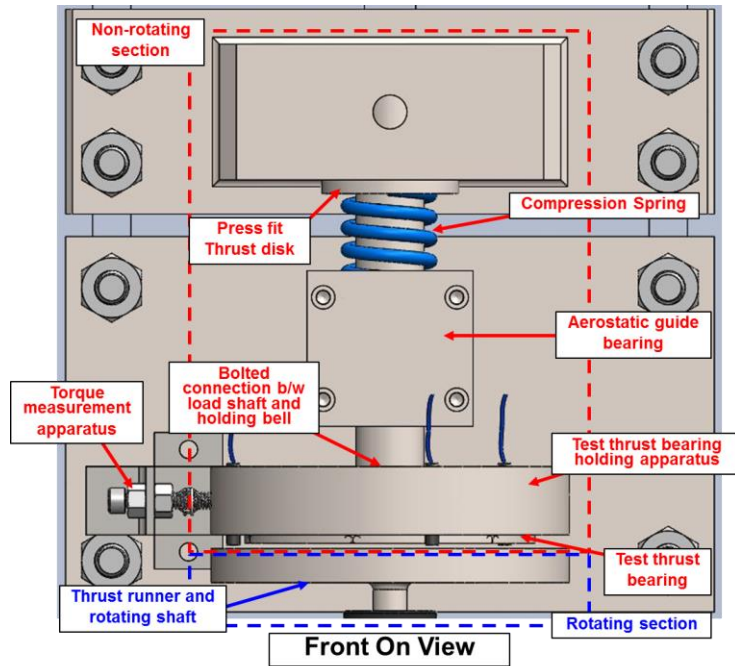
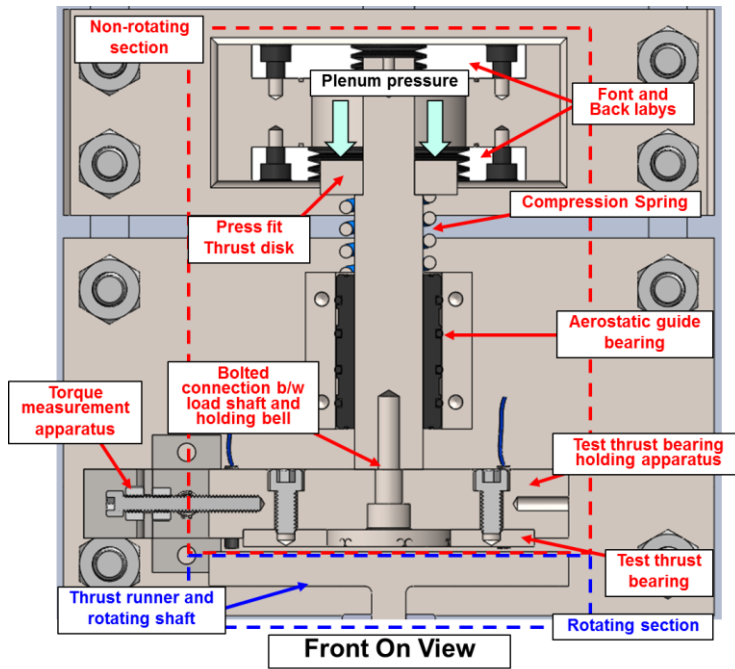


Figure 30. Schematic view of envisioned test rig for the static and dynamic evaluation of thrust foil bearings.

The static load plenum, supplied with pressurized air ($P_{max} = 1.03 \text{ MPa}$, 10.3 bar), applies a static load on the non-rotating shaft via a press fit thrust disk. Two labyrinth seals limit the leakage from the static loading plenum, and with the aerostatic guide bearing, center the non-rotating shaft such that it slides frictionless for dynamic load excitations. The maximum pressure to the plenum as well as the size of the thrust disk allow static unit loads up to $W/A_{bearing} \sim 207 \text{ kPa}$ (30 psi) for thrust bearings with outer diameters up to 114 mm (4.5 in). Figure 31 displays close up and cut section views of the static loading assembly, indicating the major components and the direction of the static load.



(a) Schematic view of the loading plenum and static loading shaft



(b) Cross section view of the loading plenum applying a static load on the test bearing

Figure 31. (a) Schematic and (b) cross section views of the static loading plenum and shaft for a thrust bearing test rig.

An electromagnetic shaker can be installed on top of the load shaft, via a threaded connection, to apply a dynamic load in series with the static load from the plenum. Measuring the displacement of the thrust bearing, relative to the rotating thrust runner, along with the applied dynamic force and the acceleration of the bearing would yield the thrust bearings dynamic load performance.

In addition to static load versus deflection and dynamic performance, the test rig will include provisions for measuring the minimum film thickness, bearing temperature rise and drag torque during startup and airborne operation.

CLOSURE

The technical report relates an improved manufacturing process for making a MM pad and method for determining their thickness. Five copper mesh pads, constructed with the mentioned method and tools herein, display similar static and dynamic load structural behavior. Thus, the procedures and tools developed for the large metal mesh bearing accomplish one of the tasks from the outset of the project.

Dynamic load measurements for the five copper mesh pads identify an average metal mesh stiffness coefficients of ~ 1.75 MN/m and material loss factor (γ) of ~ 0.2 for dynamic motion amplitude of $|\bar{X}| = 10$ μm and preload $W = 60$ N ($W/A_{pad} = 14$ kPa). Results for increasing preload (7-28 kPa) reveal that the metal mesh pad stiffness coefficient increases linearly with the applied preload. In addition, the identified pad stiffness decreases linearly with an increase in the amplitude of motion (from 5-15 μm). The results show that the individual pads have a small loss factor ($\gamma \sim 0.2$). Despite changes in the metal mesh stiffness (with motion amplitude or preload), a pad loss factor remains relatively constant (decreasing slightly with increasing excitation frequency).

Future work intends to test the large assembled MMFB in a dedicated radial gas bearing test rig capable of a shaft speed up to 40 krpm ($\Omega \frac{D_{o,R}}{2} \sim 190$ m/s surface speed).

In addition to tests with a radial MMFB, the goals for the next year include the manufacturing of both a test rig for the evaluation of foil thrust bearings as well as a novel metal mesh thrust bearing (design not forwarded in this work). The promise of metal mesh as a foil bearing support structure still exists and needs to be thoroughly assessed for both radial and thrust bearings with the push for clean energy and oil-free turbomachinery.

REFERENCES

- [1] Childs, D., 1978, "The Space Shuttle Main Engine High-Pressure Fuel Turbopump Rotordynamic Instability Problem," ASME J. Eng. Gas Turbines Power, **100**, pp. 1-10.
- [2] Zarzour, M. and Vance, J., 2000, "Experimental Evaluation of a Metal Mesh Bearing Damper," ASME J. Eng. Gas Turbines Power, **122**, pp. 1-4.
- [3] Alkhateeb, E.M., 2002, "Design, Modeling and Experimental Investigation of Mesh Vibration Dampers," Ph.D. Dissertation, Department of Mechanical Engineering, Texas A&M University.
- [4] Choudhry, V.V. and Vance, J.M., 2005, "Design Equations for Wire Mesh Bearing Dampers in Turbomachinery," Proc. ASME Turbo Expo 2005, GT2005-68641, Reno-Taho, Nevada, pp. 1-9.
- [5] San Andrés, L., Chirathadam, T. A. and Kim, T.H., 2010, "Measurement of Structural Stiffness and Damping Coefficients in a Metal Mesh Foil Bearing," ASME J. Eng. Gas Turbines Power, **132**, pp 1-7.
- [6] Chirathadam, T. A., and San Andrés, L., 2012, "A Metal Mesh Foil Bearing and a Bump Type Foil Bearing: Comparison of Performance for Two Similar Size Gas Bearings," ASME J. Eng. Gas Turbines Power, **134**, pp. 10250.
- [7] Ertas, B., Luo, H. and Hallman, D., 2009, "Dynamic Characteristics of Shape Memory Alloy Metal Mesh Dampers," 50th AIAA Structures, Structural Dynamics, and Materials Conference, May, Palm Springs, California, pp. 1-8.
- [8] Ertas, B., 2009, "Compliant Hybrid Journal Bearings Using Integral Wire Mesh Dampers," ASME J. Eng. Gas Turbines Power, **131**, pp. 1-11.
- [9] Delgado, A., 2015, "Experimental Identification of Dynamic Force Coefficients for a 110 mm Compliantly Damped Hybrid Gas Bearing," J. Eng. Gas Turbines Power, **137**, pp 1-8.
- [10] De Santiago, O. and Solórzano, V., 2013, "Experiments with Scaled Foil Bearings in a Test Compressor Rotor," Proc. ASME Turbo Expo, June, San Antonio, Texas, GT2013-94087, pp. 1-8.
- [11] Feng, K., Liu, W., Zhang, Z. and Zhang, T., 2016, "Theoretical Model of a Flexure Pivot Tilting Pad Gas Bearings with Metal Mesh Dampers in Parallel," Tribology International, **94**, pp. 26-38.
- [12] Feng, K., Zhao, X., Zhang, Z. and Zhang, T., 2016, "Numerical and Compact Model of Metal Mesh Foil Bearings," STLE Trib. Trans., **59** (3), pp. 480-490.
- [13] San Andrés, L. and Cable, T.A, 2015, "Identification of Structural Stiffness and Material Loss Factor in a Large Diameter Metal Mesh Foil Bearing," Report to the Turbomachinery Research Consortium, TRC-B&C-03-15, May.
- [14] Lee, Y.B., Kim, C.H., Kim, T.H. and Kim, T.Y., 2012, "Effects of Mesh Density on Static Load Performance of Metal Mesh Foil Bearings," ASME J. Eng. Gas Turbines Power, **134**, pp. 1-8.
- [15] TWP Inc., 2016, "Copper Wire Mesh", from <http://www.twpinc.com/wire-mesh-material/copper>.
- [16] Beckwith, T.G., Marangoni, R.D. and Lienhard, J.H., 2007, *Mechanical Measurements*, 6th Edition, Pearson Prentice Hall, Upper Saddle River, NJ, ch. 3, pp. 56-58.

- [17] Balducchi, F., Arghir, M., Gauthier, R. and Renard, E., 2013, “Experimental Analysis of the Start-Up Torque of a Mildly Loaded Foil Thrust Bearing,” ASME J. Trib., **135**, pp. 1-7.
- [18] Balducchi, F., Arghir, M. and Gauthier, R., 2015, “Experimental Analysis of the Dynamic Characteristics of a Foil Thrust Bearing ,” ASME J. Trib., **137**, pp. 1-9.

APPENDIX A: UNCERTAINTY ANALYSIS

A 95% confidence interval and a standard t distribution calculates the variability (precision uncertainty) in the real and imaginary parts of the complex stiffness \bar{F}/\bar{X} . Equation (A1) gives the precision uncertainty for a small sample size (n) and for a certain level of confidence (c)

$$P_x = t_{\alpha/2, \nu} \frac{S_x}{\sqrt{n}} \quad (\text{A1})$$

where $t_{\alpha/2, \nu}$ is a set t -statistic for $\nu = n - 2$ degrees of freedom and S_x is the standard deviation of the data set.

As an example, Table A.1 displays the real parts of the complex stiffness for Pad #5, for a motion amplitude $|\bar{X}| = 10 \mu\text{m}$ and a preload $W = 60 \text{ N}$ (data presented graphically in Figure 18(a)). The real part of the complex stiffness at each frequency represents the average of 10 individual excitations, thus, $\nu = n - 2 = 8$ and the corresponding t -statistic $t_{\alpha/2, \nu} = 2.306$. Table A.1 displays the variability (precision uncertainty) P_x in the real part of the complex stiffness, showing that the ten measurements (at each frequency) are nearly identical.

Table A.1 Real parts of the complex stiffness and their associated precision uncertainties for a confidence interval of 95%. Pad #5, $|X| = 10 \mu\text{m}$, $W = 60 \text{ N}$.

Frequency [Hz]	30	60	90	120	150	180	210	240	270	300
$\text{Re}(\bar{F}/\bar{X})$ [MN/m]	1.74	1.43	0.82	-0.24	-1.16	-2.42	-3.86	-5.42	-6.92	-8.57
P_x [MN/m]	0.001	0.003	0.004	0.004	0.005	0.010	0.014	0.018	0.022	0.029

As in the body of the report $\text{Re}(\bar{F}/\bar{X}) \rightarrow -M\omega^2 + K_{eq}$, thus a least squares method fits the data to determine the equivalent mass and stiffness coefficients. As with the

measurements, there is uncertainty associated with the slope and intercept of the least squares fit ($y = a + bx$), and given by

$$a \pm \left(t_{\alpha/2, \nu} \cdot s_{y/x} \sqrt{\frac{1}{n} + \frac{x_m^2}{S_{xx}}} \right), \quad b \pm \left(t_{\alpha/2, \nu} \frac{s_{y/x}}{S_{xx}} \right) \quad (\text{A2})$$

where the terms $s_{y/x}$, S_{xx} , and x_m are as defined in Appendix F of Ref. [16]. Table A.2 displays the equivalent mass and stiffness coefficients determined with a least squares fit of the data presented in Table A.1. In addition to the determined coefficients, Table A.2 also presents the precision uncertainty (at a 95% confidence interval) for the extracted coefficients.

Table A.2 Equivalent stiffness and mass for Pad #5 and associated uncertainties for a 95% confidence interval. $|X| = 10 \mu\text{m}$, $W = 60 \text{ N}$.

	Curve Fit	Uncertainty	%
Equivalent Stiffness, K_{eq} [MN/m]	1.61	0.29	18
Equivalent Mass, M [kg]	2.98	0.17	5

The metal mesh stiffness coefficient ($K_{MM} = K_{eq} - 2K_s \sim K_{eq}$) and the imaginary part of the complex stiffness determines a material loss factor. In Eq. (A3), $x_1 = \text{Im}(\bar{F}/\bar{X})$ and $x_2 = K_{MM}$.

$$\gamma = \frac{\text{Im}(\bar{F}/\bar{X})}{K_{MM}} = \frac{x_1}{x_2} \quad (\text{A3})$$

A standard Kline-McClintock approach determines the propagation of uncertainty to the loss factor (γ).

$$u_\gamma = \sqrt{\left(\frac{\partial \gamma}{\partial x_1} u_{x_1} \right)^2 + \left(\frac{\partial \gamma}{\partial x_2} u_{x_2} \right)^2} \quad (\text{A4})$$

Table A.3 displays the calculated loss factors for Pad #5 for a motion amplitude $|\bar{X}| = 10 \mu\text{m}$ and a preload $W = 60 \text{ N}$ (data presented graphically in Figure 19). In addition to the loss factors, Table A.3 displays the uncertainty (u_γ) for the loss factor at each excitation frequency.

Table A.3 Material loss factors and their associated precision uncertainties for a confidence interval of 95%. Pad #5, $|X| = 10 \mu\text{m}$, $W = 60 \text{ N}$.

Frequency [Hz]	30	60	90	120	150	180	210	240	270	300
$\gamma = \frac{\text{Im}(\bar{F}/\bar{X})}{K_{MM}} [-]$	0.26	0.34	0.25	0.22	0.23	0.22	0.19	0.36	0.13	0.16
$u_\gamma [-]$	0.05	0.06	0.05	0.04	0.04	0.05	0.05	0.08	0.05	0.06